

X-ray computed tomography analysis of pore deformation in IN718 made with directed energy deposition via in-situ tensile testing

Orion L. Kafka^{a,b,d}, Cheng Yu^a, Puikai Cheng^a, Sarah J. Wolff^a, Jennifer L. Bennett^a, Edward J. Garboczi^b, Jian Cao^a, Xianghui Xiao^c, Wing Kam Liu^a

^a*Department of Mechanical Engineering, Northwestern University*

^b*National Institute of Standards and Technology, Material Measurement Laboratory, Applied Chemicals and Materials Division*

^c*National Synchrotron Light Source II, Brookhaven National Laboratory*

^d*Corresponding author: olkafka@u.northwestern.edu, orion.kafka@nist.gov*

Abstract

Directed energy deposition (DED) is a metal additive manufacturing technique often used for larger-scale components and part repair. It can result in material performance that differs from conventionally processed metal. This work studies spatial and orientation-based differences in tensile properties of nickel-based alloy IN718 using *in-situ* x-ray computed tomography to observe internal pore populations. Anisotropy and spatial variability in mechanical properties are shown while the evolution of pore shape during deformation is measured. Measured pore deformation is compared to predict deformations simulated using a computational crystal plasticity scheme, which provides insight, through inverse modeling, to the grain orientation in which the pore resides. The measurements provide a high fidelity method to compare experimental and computational approaches to pore deformation studies. Pore deformation measurements show that pores tend to grow and elongate in the direction of loading, consistent with ductile deformation and likely deforming with the material. Generally, the pore defects observed in this material (not from lack-of-fusion) do not cause so-called premature failure, and fully developed necking occurs prior to fracture.

Keywords: Additive manufacturing, Directed energy deposition, Tensile testing, Mechanical property variations, In-situ X-ray CT, Pore mechanics, Model verification

1. Introduction

Many metal additive manufacturing (AM) technologies exist, and each has different material impacts and associated challenges. The work presented here relates specifically to the directed energy deposition (DED) AM technique, where powder is delivered with a shielding gas to a molten pool created by a laser. This can offer more flexibility than powder-bed type AM, with applications such as repair and large area manufacturing possible as described by Shamsaei et al. (2015); Zhai et al. (2019). The cooling rate typical in DED is between that

8 experienced by conventional casting and powder-bed AM material, meaning that a unique
9 set of microstructures can occur. A variety of other differences in length and time scales
10 mean that the performance of DED-built material is not necessarily similar to cast, wrought,
11 or powder-bed AM processed material, c.f. [Sochalski-Kolbus et al. \(2015\)](#); [Schneider \(2020\)](#);
12 [Xavier et al. \(2020\)](#); [Gordon et al. \(2019\)](#). Thus, a body of literature related specifically to
13 DED-type processes, and the different alloys used in these processes, needs to be developed
14 to enable confident use of DED materials in structural and high performance applications,
15 such as in structural, aeronautical components [Gorelik \(2017\)](#).

16 This paper first presents an experimental study that focuses on observational and quanti-
17 tative measurement of the deformation of pores in DED-built nickel-based super-alloy IN718,
18 and pairs this with a computational crystal plasticity analysis of the pore deformation pro-
19 cess. IN718 is a commonly used alloy in AM applications, and is relatively easy to process
20 with a laser, because it is precipitation-hardened and quench-suppressible, meaning that
21 it can be deposited and possibly finish-machined in a more malleable state and later heat
22 treated to achieve full strength. This Ni-Fe alloy is used in applications such as gas turbines,
23 space craft, and nuclear reactors because it has high strength, fatigue strength, and corrosion
24 resistance, as well as high creep-rupture strength at elevated temperatures [Zhai et al. \(2019\)](#).

25 Previous studies have identified significant anisotropy and variability in as-built, stress-
26 relieved, and heat treated DED IN718, as well as sub-standard material performance, as
27 shown in [Liu et al. \(2011a\)](#); [Li et al. \(2020\)](#); [Zhang et al. \(2020\)](#); [Glerum et al. \(2021\)](#). Reports
28 have, however, varied with some authors finding wrought-equivalent properties particularly
29 after heat treatment [Qi et al. \(2009\)](#); [Lambarri et al. \(2013\)](#). It has been known for perhaps
30 10 years that the microstructures and mechanical properties of IN718 depend on many factors
31 in the DED process, including feedstock, process parameters, scan strategy, build conditions,
32 and post-build treatments [Liu et al. \(2011a\)](#); [Blackwell \(2005\)](#); [Liu et al. \(2011b\)](#); [Parimi
33 et al. \(2012\)](#). Process monitoring, real-time control, secondary processes, heat treatments,
34 and other techniques can be used to mitigate the worst difficulties with the method, and

35 efforts have been made to in this direction. However, processing defects and particularly
36 microscale pores and undesirable phases can still occur [Bennett et al. \(2017\)](#); [Wolff et al.](#)
37 [\(2019\)](#); [Gan et al. \(2019\)](#); [Sui et al. \(2019\)](#); [Jinoop et al. \(2019\)](#); [Ning et al. \(2018\)](#); [Qi et al.](#)
38 [\(2009\)](#); [Zhong et al. \(2016\)](#); [Yuan et al. \(2018\)](#); [Zhao et al. \(2008\)](#). Indeed, several parallel
39 studies to the current work by the same team have recently appeared, focusing on techniques
40 to avoid these factors and specifically employing tests on thin wall specimens similar to those
41 described below, though with a focus on the thermal processing and microstructural aspects
42 rather than the present focus on pores and their deformation mechanisms [Glerum et al.](#)
43 [\(2021\)](#); [Bennett et al. \(2021\)](#).

44 Mechanical testing with *in-situ* inspection has been used in prior works to assess how
45 microstructures deform during loading, and in particular how the unique features generated
46 by AM processing impact performance. For example, [Carlton et al.](#) studied deformation of
47 316L Stainless Steel with a range of pore defect sizes, concluding that, for relatively dense
48 material, conventional failure processes dominate while for specimens with large pores (the
49 largest was $1100.0 \times 10^4 \mu\text{m}^3$) a defect-driven mode would dominate [Carlton et al. \(2016\)](#).
50 Similarly, [Voisin et al.](#) used *in-situ* x-ray diffraction and post-mortem XCT to study the
51 deformation mechanics of AM Ti-6Al-4V, and the impact that even a small volume frac-
52 tion of pores (i.e. $\ll 1 \text{ vol}\%$) has on total strain to failure [Voisin et al. \(2018\)](#). [Kim et al.](#)
53 used lab-scale XCT to measure the evolution of artificially created internal defects in AM
54 17-4 Stainless Steel, and showed quantitatively that pore growth drives increasing stress
55 concentrations that ultimately result in failure [Kim et al. \(2020\)](#). More broadly XCT is
56 an important inspection tool that can be useful for discriminating between dangerous and
57 harmless defects, and advancing understanding of the effect of pores on mechanical prop-
58 erties [du Plessis et al. \(2020\)](#). XCT has been instrumental in developing an understanding
59 of the role of pore defects in the mechanical properties of metals, including AM metals in
60 the last 15 years including but not limited to: [Steuwer et al. \(2006\)](#); [Steuwer and Daniels](#)
61 [\(2011\)](#); [Maire et al. \(2007\)](#); [Landron et al. \(2011\)](#); [Weck et al. \(2008\)](#); [Limodin et al. \(2010\)](#);

62 [Toda et al. \(2011\)](#); [Lecarme et al. \(2014\)](#); [Nguyen et al. \(2016\)](#); [Krakhmalev et al. \(2016\)](#);
63 [Patterson et al. \(2018\)](#); [Samei et al. \(2020\)](#); [Hastie et al. \(2021\)](#).

64 Although [Hosseini et al.](#) propose several mechanisms for varying properties between ori-
65 entations and builds (including pores and grain boundary density), no direct evidence was
66 provided [Hosseini and Popovich \(2019\)](#). To further explore the proposed mechanisms, we
67 specifically studied pores undergoing uniaxial tension and ductile deformation to understand
68 if, and how, pore defects impact deformation behavior of DED IN718. Broadly, pore defor-
69 mation can be an important aspect of deformation, including the development of damage
70 and failure. Our work develops a deeper understanding of how deformation progression al-
71 ters pore shape and size (both individually and in aggregate) through direct observation and
72 statistical image analysis during pre-failure deformation. Moreover, the *in-situ* deformation
73 measurements presented here can be effectively used for image-based model verification, en-
74 hancing our confidence in the accuracy and precision of models that attempt to capture pore
75 deformation during plastic deformation. This is particularly helpful for models, especially
76 multiscale models, that directly represent microscale features, such as measured pores or
77 simulated grain structures [Kafka et al. \(2021\)](#); [Yu et al. \(2019\)](#); [Herroitt et al. \(2019\)](#); [Li](#)
78 [et al. \(2019\)](#); [Yan et al. \(2018\)](#).

79 The manuscript is arranged into five main sections: section 2 describes the materials and
80 manufacturing methods used; section 3 describes in detail the *in-situ* testing and imaging
81 protocols; section 4 provides results and discussion; section 5 uses crystal plasticity modeling
82 to determine the local grain orientation surrounding a pore, with a comparison of pore shapes
83 between the numerical model and 3D imaging results. This section emphasizes the utility of
84 direct, *in-situ* observation of pore deformation in relationship to micromechanical modeling.
85 Finally, section 6 provides concluding remarks, including thoughts on future studies.

86 2. Materials and Methods

87 In this study, we focused on DED IN718, which was argon gas atomized to a particle size
88 of 50 μm to 150 μm with a Gaussian distribution, before being used for the builds. All three
89 builds studied here used the same batch of powder.

90 2.1. AM build details

91 Three single-track, “thin wall,” builds using a DMG MORI LaserTec 65 3D Hybrid¹ were
92 deposited on stainless steel grade 304 substrates. Thin walls are a simplified geometric case
93 that minimize potential variables (such as removing the possibility of “lack of fusion” type
94 defects) compared to a more complex build, while also enabling more direct observation of
95 the build using side-on optics. The tool uses a direct diode laser, in this case operated at
96 1800 W, 1020 nm wavelength, and approximately 3 mm focal spot size. Each single-track
97 build resulted in a wall nominally 120 mm long, 60 mm high, and about 3.5 mm thick. Argon
98 shield and conveying gas at 7 L/min protected the melt pool while delivering powder coaxially
99 to the laser. Three walls were built with different build patterns; each wall was built using
100 a zig-zag scan strategy with a layer height of 0.5 mm and 1000 mm/min scan speed, but
101 two walls shared a 18.0 g/min powder mass flow rate (PMFR) while the third had about
102 a 27.0 g/min PMFR. Using the basic definition of Global Energy Density (GED) $GED =$
103 $\frac{\text{power}}{(\text{scanSpeed})(\text{laserRadius})}$ Kruth et al. (2005), the nominal GED of all three builds was 0.01 J/mm²;
104 however, because this is a thin wall build (and lacks hatch spacing), it may not be comparable
105 to other GED measurements. Of the two walls with the same PMFR, one had no dwell time
106 between layers and one had a 60 s dwell between layers. Differences in microstructure for
107 similar thin wall structures with differences in dwell time have recently been reported (likely
108 due to different cooling rate and residual heat), indicating that differences in mechanical

¹Certain commercial equipment, software and/or materials are identified in this paper in order to adequately specify the experimental procedure. In no case does such identification imply recommendation or endorsement by the National Institute of Standards and Technology, nor does it imply that the equipment and/or materials used are necessarily the best available for the purpose.

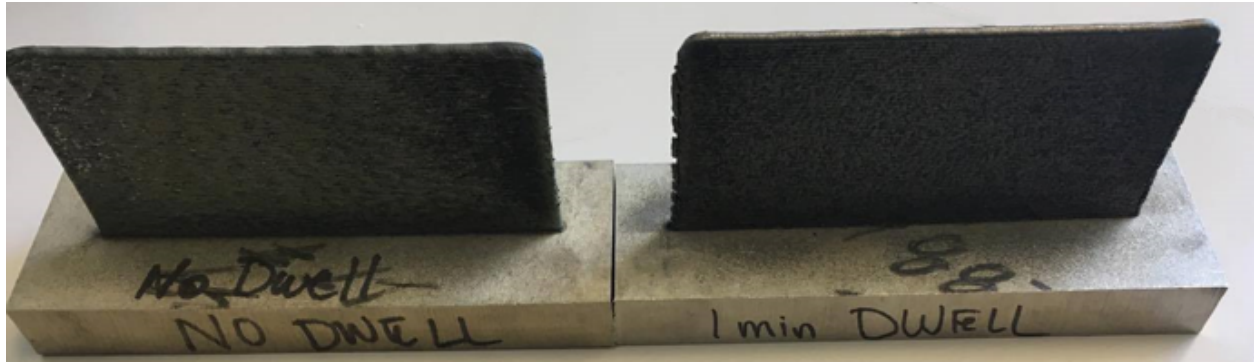


Figure 1: A photography of two of the thin walls (Wall 3 (left) and Wall 2 (right)) that were then cut up to make miniature tensile coupons. Note there are noticeable geometry inaccuracies, even from this perspective.

109 performance may be expected [Guévenoux et al. \(2020\)](#). Real-time thermal monitoring for
110 these walls has in part been reported in Bennett *et al.* [Bennett et al. \(2018\)](#). For these builds,
111 the scan direction was taken to be along the length of the wall, the “hatch” or thickness
112 direction is the thickness (although there is no hatching in the thin walls), and the build
113 direction is the height away from the base plate, as indicated in Figure 2.

114 After building, a 1 h at 1065 °C stress-relieving heat treatment followed by air cooling to
115 room temperature was conducted, per AMS standard 5664F. It is important to note that this
116 is a solutionizing heat treatment; a precipitation heat treatment was not conducted, although
117 in practice is often used. The goal of the heat treatment was to reduce residual stress and
118 enable removal of the build from the substrate without warping. This heat treatment likely
119 solutionized precipitate phases from the build itself (predominately γ'' and Laves), but was
120 unlikely to cause significant recrystallization [Sui et al. \(2019\)](#). The specimens were eventually
121 tested in the solutionized and air cooled state.

122 A photograph of two of the thin walls prior to stress relief in Figure 1 shows their as-
123 built shape, including inexact geometric features such as slightly warped top and side surfaces
124 and rounded corners that result from the process. This meant that any absolute real-space
125 position measurements with respect to the programmed geometry had some unavoidable
126 inaccuracy.

127 *2.2. Specimen selection and preparation*

128 Miniaturized ASTM E8 pin-loaded tensile coupons with nominal gauge section 2.5 mm
129 long, 1.2 mm wide, and 0.8 mm thick (see Figure 4) were designed for these tests. The ge-
130 ometry proved successful, in that most failures occurred in the gauge region, minimal strain
131 was observed in the grip regions, and surface DIC indicated generally uniaxial strain states.
132 Specifically, shear strains in the elastic region in the specimens were observed to be small
133 (generally $<5\%$) compared to the axial strains as measured by 2D-DIC, indicating relatively
134 high uniaxiality. Specimens were exhumed from each wall using wire electric discharge ma-
135 chining (wire-EDM) to minimize disturbance of the material prior to testing. Wire-EDM
136 can, however, leave a porous re-cast material layer, e.g. [Markopoulos et al. \(2020\)](#), which
137 was observed in XCT to contain relatively higher porosity than the undisturbed material.
138 The small size makes these specimens similar in concept to recent work in miniaturized
139 testing of AM materials such as that of [Benzing et al. \(2020\)](#), and builds a
140 case for the utility of sub-scale mechanical testing for AM materials. The smaller geometry
141 might inherently result in different measurements than full size coupons, although in some
142 cases miniaturized specimens may provide similar results [Anderson et al. \(2017\)](#). In any
143 case, for this study using small specimens was necessary in order to understand the possible
144 distribution of properties within each wall. With little *a priori* knowledge of the distribu-
145 tion of properties within the walls, a Sobol sequence was used to define the points at which
146 the specimens were collected from the walls. The Sobol sequence maximized the informa-
147 tion gathered on the underlying spatial distribution of properties measured within the walls
148 [Burhenne et al. \(2011\)](#), which reduces testing requirements when compared to, e.g., random
149 sampling. To test for anisotropy, half the coupons were exhumed with the gauge section
150 parallel to the build direction and half perpendicular to the build direction. To maximize
151 the similarity, in terms of processing history, between the horizontal and vertical specimens
152 and eliminate possible differentiating variables, the roughly 3 mm thick wall was sectioned
153 longitudinally to produce two 0.8 mm to 1 mm thick sheets (changes in thickness resulted

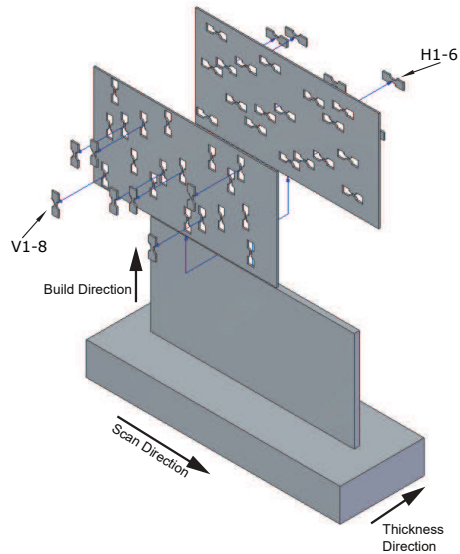


Figure 2: Coupon locations in each thin wall (single laser track) build, with two labeled examples

154 from unavoidable warping during removal from the build substrate). Horizontal and vertical
 155 specimens were then cut from the same coordinates of each sheet, such that the distance be-
 156 tween gauge sections in the precursor material was minimized. Due to the symmetric nature
 157 of the single-track thin wall, through-thickness variability was minimal and the specimens
 158 are generally similar between sides as confirmed by grain, pore, and mechanical properties
 159 comparisons. This specimen extraction and overlap-gauge-section concept is shown schemat-
 160 ically in Figures 2 and 3. A local specimen coordinate system with x aligned along the tensile
 161 axis, y parallel to the front/back plane of the specimen, and z into the thickness direction
 162 was used to simplify analysis. Thus, for the horizontal specimens local x strain implies strain
 163 in the scan direction, whereas for the vertical specimens, x strain implies strain in the build
 164 direction relative to the build coordinate system.

165 2.3. Surface preparation

166 To remove possible effects of the wire-EDM specimen cutting procedure, the specimens
 167 were chemically processed after machining. All specimens were immersed for approximately

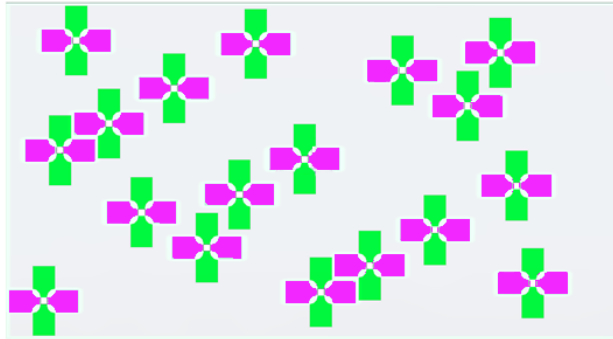


Figure 3: Relative locations and orientations of tensile specimens. Green are vertical (long axis aligned with the build direction, which is vertical in this schematic), and purple are horizontal (long axis along the scan direction).

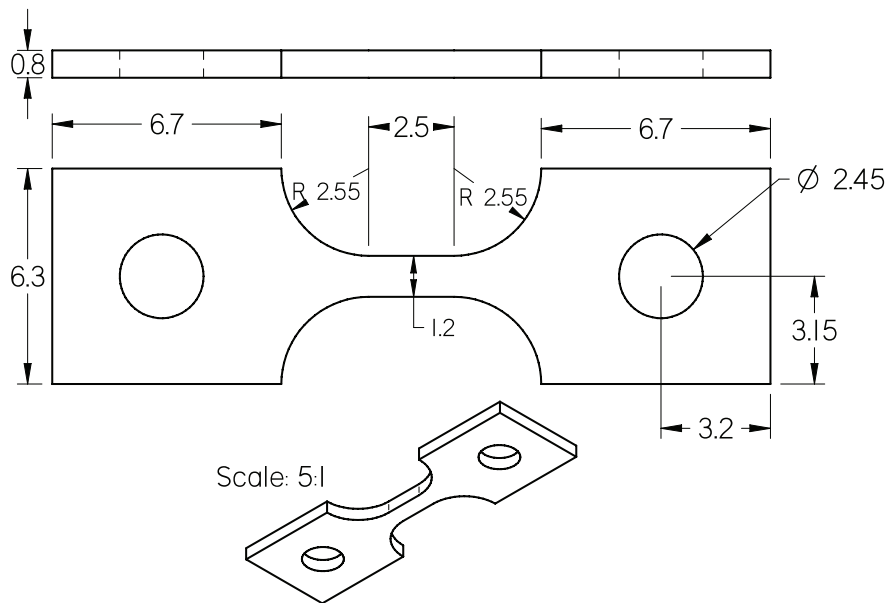


Figure 4: Details of nominal miniature specimen geometry, dimensions in mm

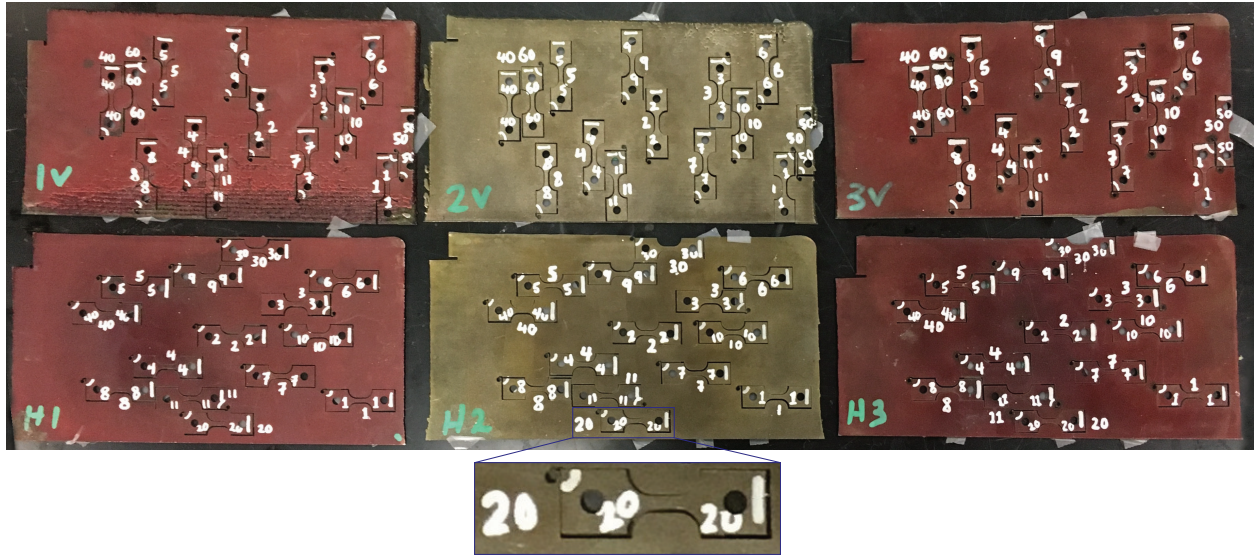


Figure 5: Labeled specimens in their respective thin wall slices prior to testing, and a more detailed view of one particular specimen showing real geometry in the build plate after wire-EDM machining.

168 90 min in Kalling's Etchant (a proportionate mix of 5 g CuCl_2 + 100 cc HCl + 100 cc Ethyl
 169 alcohol [Small et al.](#)), which removed about $50\ \mu\text{m}$ (0.05 mm) of surface material from all
 170 faces. Prior to immersion, both pin-connector ends of each specimen were coated in etch-
 171 resist, which was subsequently removed. This procedure proved insufficient to completely
 172 eliminate the re-cast wire-EDM layer, and some amount of surface porosity likely due to the
 173 wire-EDM process was still observed in the XCT results.

174 After this, caliper measurements of all specimens were taken, with three repeat measure-
 175 ments at three locations along the gauge section in each dimension (width measured with
 176 calipers, thickness with micrometers). These were used to compute cross-sectional area for
 177 engineering stress calculations prior to conducting XCT measurements. Dimensional uncer-
 178 tainty associated with caliper and micrometer fidelity, and its impact on stress uncertainty,
 179 was propagated from these measurements to the stress-strain curves. An image of the spec-
 180 imens prior to testing is shown in Figure 5, where each specimen is uniquely labeled using a
 181 letter/number convention that will be referenced in later sections. The first character, H or
 182 V, refers to the orientation (horizontal or vertical) with respect to the build direction. The
 183 second character refers to the wall: 1 = 27 g/min (0.45 g/s) PMFR, no dwell; 2 = 18 g/min

Table 1: Summary of specimen labeling scheme.

Position in label	Possible entries	Description
First	H/V	Horizontal or vertical
Second	1/2/3	Wall number: 1 = 27 g/min PMFR, no dwell; 2 = 18 g/min PMFR, 60 s dwell; 3 = 18 g/min PMFR, no dwell
Third	1-11, 20, 30, 40, 50, 60	Specimen number within wall, sorted by Sobol order

184 PMFR (0.3 g/s), 60 s dwell; 3 = 18 g/min (0.3 g/s) PMFR, no dwell. Finally, within each
 185 wall slice the specimens are numbered in accordance with the Sobol sequence, thus higher
 186 numbers provide decreasing returns in terms of information regarding the spatial distribu-
 187 tion. The numbers that end in a 0 were manually added after the sequencing to probe the
 188 extremes of the build, either at the top or edges of the build, where we suspected different
 189 properties might exist. The numbering scheme is summarized in Table 1.

190 The final stage of specimen surface preparation was to apply a speckle pattern to the
 191 gauge sections, to enable full-field digital image correlation measurements of the deformation.
 192 A black background with white speckles was generated using a solution of 6 μm alumina
 193 powder in ethanol applied to a still-tacky layer of matte black spray paint. Some amount
 194 of unavoidably clumping meant that the observed particles tended somewhat larger than
 195 the powder itself. Our preliminary testing showed that the resulting pattern had an ideal
 196 minimum subset size of about 60 μm when using the optical setup deployed during mechanical
 197 testing.

198 3. Mechanical testing

199 Specimens were tested *in-situ* in ambient air at Argonne National Laboratory’s Advanced
 200 Photon Source Beamline 2-BM. A custom-built, remotely controllable, single-sided, minia-
 201 ture screw-actuated load frame [Wejdemann et al. \(2010\)](#); [Efstathiou et al. \(2010\)](#) was used
 202 to conduct tensile loading within the hutch, as shown in Figure 6. Quasi-static testing was
 203 conducted under displacement control, such that a nominal initial strain rate $5 \times 10^{-4} \text{s}^{-1}$

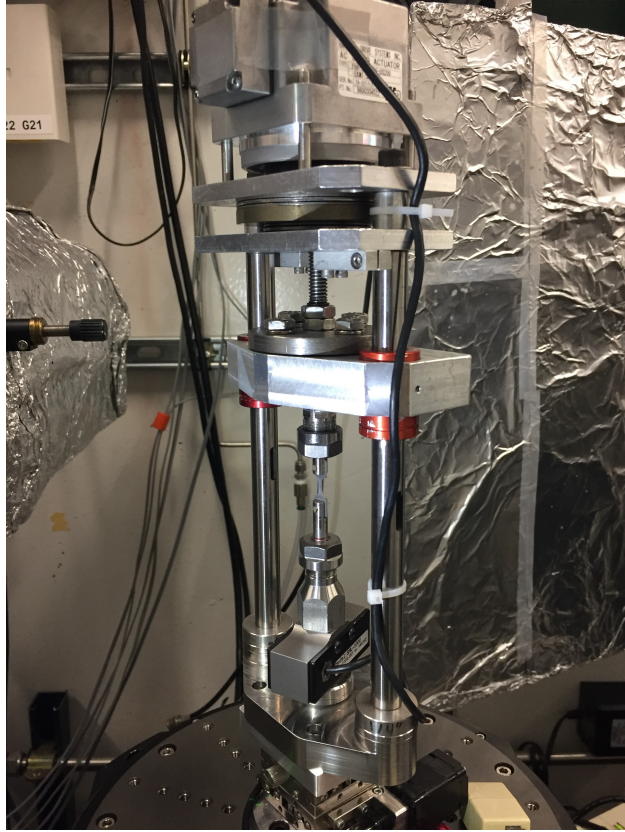


Figure 6: The miniature screw-actuated load frame used for mechanical testing, as installed on the rotary stage of Beamline 2BM-B. A specimen can be seen mounted in the pin-style clevises, themselves held with collets, which are attached on the bottom to the load cell and on the top to the movable crosshead.

204 was achieved based on initial specimen length and a continuous crosshead displacement rate.
205 This was obtained with a crosshead displacement rate of $1.25 \mu\text{m/s}$, kept constant during
206 all subsequent deformation steps for both the continuous and interrupted loading cases de-
207 scribed below. At these strain rates, this material is relatively rate-insensitive, so the steadily
208 decreasing strain rate caused by using a fixed displacement rate was assumed to have a min-
209 imal influence. Displacement was applied only one side of the specimen, while the other
210 side was held fixed, resulting in the gradual motion of the specimen through the frame of
211 view of the DIC camera as well as motion of the volume inspected by XCT. Some motion
212 mitigation for XCT viewing was attempted, although with this hardware configuration it
213 was ad-hoc and no assurance can be made that the field of view does not change during the
214 large deformations that the specimen undergoes.

215 3.1. Continuous and interrupted loading

216 Two different displacement-controlled testing protocols were used. An interrupted *in-situ*
217 modality was employed to enable XCT imaging at pre-defined points during deformation
218 (similar to, e.g., Maire et al. (2007), Carlton et al. (2016), and Kim et al. (2020), although
219 specifically designed for our specimens), and a continuous loading through failure was used to
220 enable more direct comparison to standard E8 tests of IN718. The concept of incremental and
221 continuous *in-situ* testing is not new, see for example Maire et al. (2007) for an example with
222 a specialized aluminum metal matrix composite, but still deserves thorough description. In
223 the former, displacement was applied at a constant rate to the specimen until an engineering
224 stress of 575 MPa was reached. This was usually quite close to the yield stress. At this point,
225 deformation was stopped for approximately 8 min (about 480 s). This allows about four to
226 five minutes of creep, during which time settings, file paths, etc. are manipulated as required.
227 At this point, the creep rate is low enough to conduct a 3.5 min scan without specimen motion
228 causing artifacts (i.e., we computed that on average a pore would move less than 0.65 μm ,
229 one voxel, during the scan). After the scan, displacement was increased again until stress had
230 increased by 75 MPa, at which point another pause followed by another scan was conducted.
231 This procedure of load-wait-scan was repeated until the ultimate tensile strength was reached.
232 At this point, due to the more rapid change in behavior during the softening regime, scans
233 were taken after every 15 MPa of load drop. The displacement versus time graph is shown
234 in Figure 7 is an example to illustrate the displacement history common for “start-stop”
235 specimens. Although the details of the test protocol were designed specifically for our test
236 conditions, a similar strategy was used by Yvell et al. Yvell et al. (2018) which showed little
237 difference for nickel-rich steel between stop-start testing and continuous testing in terms of
238 overall response. In two cases, rupture occurred during either the primary creep hold time or
239 during scanning. The continuous loading case was simply a standard tensile test to failure,
240 with XCT data collected before the test started and after failure. Although prior literature
241 is understandably scarce on the impact of interrupted *in-situ* testing on general deformation

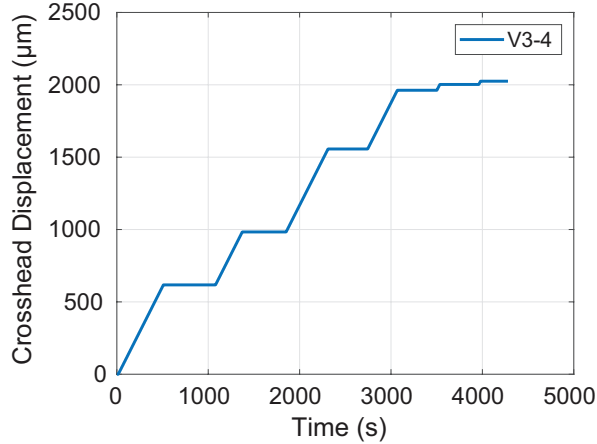


Figure 7: Crosshead displacement versus time for specimen V3-4, as an example of the “start-stop” or interrupted *in-situ* loading pattern. Constant displacement rate during crosshead motion is also demonstrated.

242 behavior and material performance of DED IN718 specifically, our results below seem to
 243 indicate limited difference for IN718 between interrupt and continuous testing, although we
 244 were unable to confidently isolate this as a variable due to the heterogeneous nature of the
 245 AM material in this study. In this case, we must be somewhat careful to avoid excessive
 246 comparison between specimens tested with interrupted versus continuous loading.

247 *3.2. Surface strain measurement with digital image correlation*

248 During deformation and at all times other than during an XCT scan (when the specimen
 249 was rotated and thus not observed by the camera), speckle pattern images of the specimen
 250 surface were collected with a Point Gray Research Grasshopper3 camera, sensor size 3376 ×
 251 2704 pixels, at 1 frame/s and with exposure time 0.5s. An Infinity K2/DistaMax long
 252 distance microscope with K2 Close-Focus Objective and CF-2 optic was used to provide
 253 detailed images of the gauge section of the miniature test specimens. A LED light panel
 254 with custom light directing hood was used to avoid influencing the x-ray detector. LED
 255 lighting does not significantly heat the specimens or surrounding air. Specular reflections
 256 were mitigated with cross-polarization, as suggested by LePage *et al.* [LePage et al. \(2016\)](#).
 257 The use of this rather bulky collection of DIC equipment was made possible by the space
 258 available in the synchrotron hutch, which is generally much larger than in lab-scale XCT

259 systems. Two-dimensional digital image correlation with the VIC 2D software package [VIC-](https://www.correlatedsolutions.com/vic-2d/)
260 [2D Version 6, Correlated Solutions, Irmo SC, https://www.correlatedsolutions.com/vic-2d/](https://www.correlatedsolutions.com/vic-2d/)
261 was used to compute surface displacement after testing. Details of the DIC settings that
262 generally provided good quality correlations for these images are provided in Table 2. Of
263 note, the tele-microscope lens does not have fixed f-stops and instead uses an adjustable
264 field iris. We adjusted it to achieve satisfactory image quality, lighting, and depth of field
265 for our speckle pattern and illumination. Also note that, the confidence intervals on zero-
266 displacement images will be somewhat smaller than for images taken during deformation
267 (as an approximation, the highest observed strain rate would result in about a half-pixel of
268 motion while the shutter is open). Out of plane motion was minimal, even during necking the
269 maximum possible spurious biaxial strain due to Poisson effect is approximately 1.5×10^{-3} ,
270 which is much less than the overall strains at the point of maximum out of plane motion.
271 In practice, this maximum is far from what is observed, as width reduction is on the order
272 of 50%. From the displacement, total strain was computed using both a local and a global
273 approximation from the measured displacements (both were used and compared both in
274 VIC2D and in a custom MATLAB script to help ensure accuracy). For some specimens,
275 load frame displacement was tracked and used to cross-verify the DIC results, although
276 in all cases DIC strain measurements are reported. These DIC displacements/strains were
277 registered against load cell readings by minimizing the difference in time stamp to produce
278 load vs. displacement as well as engineering stress versus engineering strain.

279 *3.3. XCT observation of porosity*

280 Tomographic measurements of the specimens were conducted at the 2-BM beamline of
281 APS at ANL. The load frame noted above was mounted on the top of a rotary stage. In
282 a tomography scan, the load frame and specimen held within it were rotated through 180-
283 degrees while an X-ray detector behind the specimen acquired 1501 projection images of the
284 specimen. The X-ray detector was composed of a 20 μm thick LuAG:Ce X-ray scintillator,
285 a 10 \times Mitutoyo long-working distance optical objective lens, and a PCO Edge5.5 sCMOS

Table 2: Optical and VIC2D DIC settings used to compute surface displacements, reported as suggested by [Bigger et al. \(2018\)](#). The 95% confidence intervals are the mean value for a representative zero displacement image pair (from V2-3) assuming normally distributed error

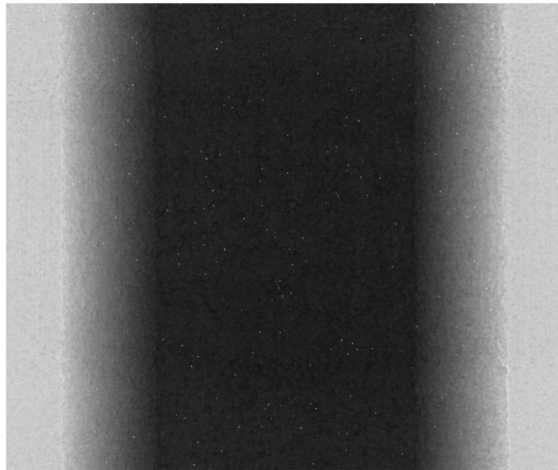
Optical parameter	Value
Camera body	Point Gray Research Grasshopper3
Sensor size, px	3376×2704
Lens	Infinity K2/DistaMax
Objective	K2 Close-Focus with CF-2
Working distance, mm	approx. 300
Image scale, pixels/mm	approx. 518
DIC parameter	Value
Software	VIC-2D Version 6.06, build 665
Subset size	35
Step size	7
Subset weights	Gaussian
Interpolation	Optimized 6-tap
Criterion	Normalized squared differences
Mode	Incremental
Consistency margin, maximum margin, px	0.02
Confidence margin, maximum margin, px	0.05
95% CI for displacement, px	[0.012, 0.081]
Matchability threshold, maximum margin	0.1
Strain computation filter size, px	15
Strain measure	Lagrange
95% CI for strain	[-8.05e-05, 6.57e-04]

286 camera, which gave an effective $0.65\ \mu\text{m}$ pixel size. The broadband, white-light X-ray from
287 the source was filtered to provide an illumination beam with peak energy about 60 keV.
288 In the scans, the two supporting arms of the load frame blocked about 20 degrees in the
289 total 180-degree angle range. The images taken in this black-out angle range were discarded
290 in the tomographic reconstructions, meaning that only 160 degrees of data were used for
291 reconstruction. A custom reconstruction technique was used to mitigate the impact of these
292 dropped frames, the details of which can be found in the related code and data publication
293 [dataset] [Kafka et al. \(2022\)](#). The exposure time of projection images was 100 ms (0.1 s),
294 and each tomographic scan took 3 min scan time and (0.5 min) scan preparation overhead
295 time. This system is shown schematically in Figure 9. For all specimens, a field of view
296 was selected that started about 0.150 mm below the upper fillet and extended 1.3975 mm
297 towards the lower fillet, capturing the upper two-thirds of the gauge section, at least before
298 deformation began. Because the load frame applies single-sided displacement, the field of
299 view was translated half the total crosshead displacement at each step to roughly maintain
300 the field of view. Specimens tested using the continuous loading protocol were scanned before
301 testing and the two sides of each broken specimen were scanned after failure using all the
302 same settings.

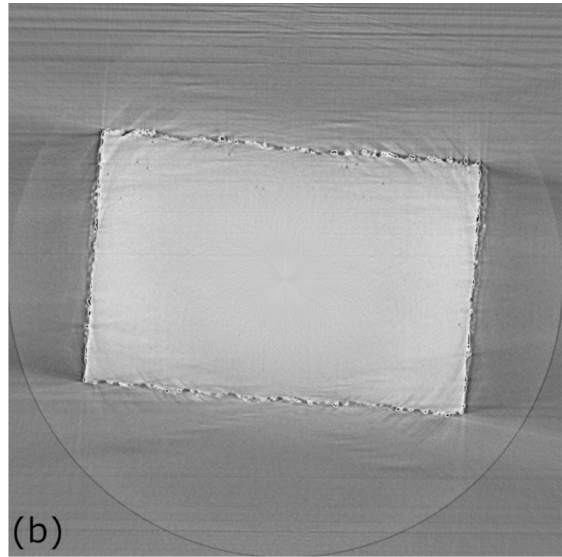
303 Tomographic reconstruction was conducted using a customized version of Tomopy 1.0.1
304 [Gürsoy et al. \(2014\)](#). The modifications were a correction of a coding error that results in the
305 program hanging during multi-processor operation and an added output to directly make an
306 8-bit tiff image rather than the standard 16-bit output (to save disk space, as there was no
307 noticeable difference in final 3D image quality for these specimens). An example initial pro-
308 jection image is shown in Figure 8a). Projection images were processed in a high-throughput,
309 parallel environment based on a combination of BASH and Python scripts. In Tomopy, the
310 projection images were normalized, followed by phase retrieval, stripe removal, and a final
311 renormalization. After reconstruction using the gridrec algorithm, range adjustment, outlier
312 removal and ring removal were conducted before saving the tiff image stack (Figure 8b)).

313 Next, a series of edge-preserving, smoothing filters to reduce noise and enhance contrast
314 between the material and pore phases were applied using the MATLAB Image Processing
315 Toolbox (version 2018b) with a series of *localcontrast*, Wiener, and median filters. Both
316 2D and 3D versions of the filters were tested, and largely similar final 3D results achieved
317 with both. So the faster 2D filters were chosen and all reported images use the same set
318 of 2D filters. After filtering, the *graythresh* and *imbinarize* functions were used to binarize
319 the images, differentiating the volume into two phases: surrounding air/pores and metal
320 (Figure 8c) and 8d)). Data from intermediate processing steps can be reproduced using the
321 associated dataset [dataset] [Kafka et al. \(2022\)](#). The voxel edge length was $0.65\ \mu\text{m}$, giving a
322 minimum detectable pore size, if we assume that two darker voxels in each direction would
323 be detectable, of about $2.197\ \mu\text{m}^3$.

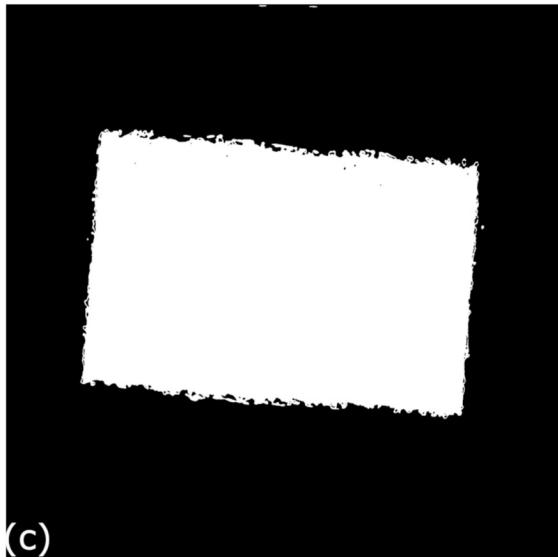
324 Overall descriptive parameters were extracted from the binary images of the material
325 using the techniques developed in [Garboczi and Hrabec \(2020a,b\)](#); [Bain et al. \(2019\)](#). In order
326 to focus upon the primary features of interest, DED-derived pores, several more processing
327 steps were required for these images. The images were first cropped and the exterior air
328 spaced turned gray. Surface pores produced by the wire-EDM process were removed by
329 conducting 30-50 dilation steps of this gray region. The gray region was turned black, leaving
330 only the internal pores. Some of these pores are likely reconstruction “ring” artifacts, caused
331 by the slightly reduced contrast in the *in-situ* XCT images due to interference from the load
332 frame. To ensure these were not included in pore evolution statistics, each pore was evaluated
333 as to whether or not its 3D shape could be expanded in spherical harmonic functions. Those
334 that could not be so expanded were removed from the analysis as probable artifacts, because
335 real pore are generally roughly spherical (recall there are no lack-of-fusion defects). Spot
336 checking with 3D images of these pores confirmed this hypothesis. The parameters L, W,
337 and T were computed for each pore analyzed, where L is the longest distance across a pore,
338 W is the longest distance that is also perpendicular to L, and T is the longest distance that
339 is also perpendicular to both L and W. The bounding box extents in image coordinates were



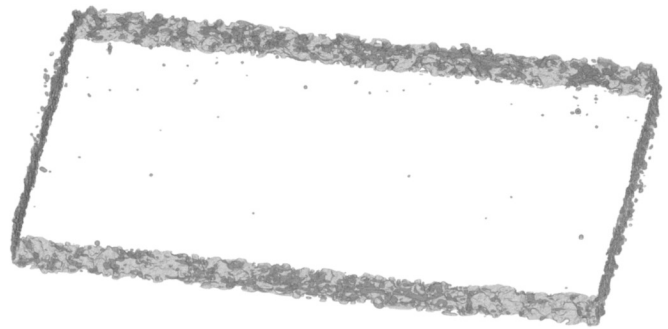
(a)



(b)



(c)



(d)

Figure 8: a) example projection image (reproduced here with an “equalized” histogram to enhance visibility, and without bright and dark field corrections), b) gray-scale reconstruction slice, c) filtered and thresholded slice, d) filtered and thresholded 100 slices around the slice shown in part c).

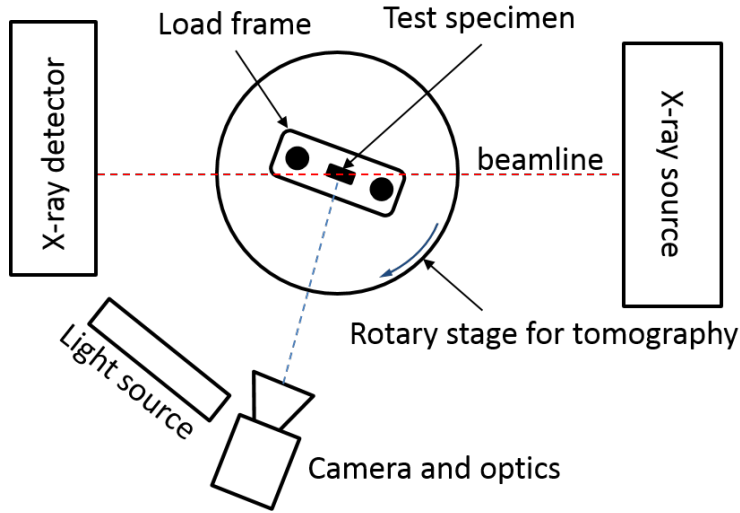


Figure 9: Schematic diagram (not to scale, top down view), of the specimen location with respect to the DIC camera and x-ray beam.

340 computed and denoted x , y , and z , where z is the loading direction.

341 4. Experimental results

342 4.1. Stress-strain curves

343 For each thin wall, at each point in strain the stress values of all the H or V specimens were
 344 averaged together. The “average” engineering stress-strain curves with shadowed regions
 345 representing ± 1 standard deviation (SD) are shown in Figure 10; (a) wall 1 (27 g/min PMFR,
 346 no dwell, continuous testing), $N_V = N_H = 10$, (b) wall 2 (18 g/min PMFR, 60 s dwell, stop-
 347 start testing), $N_V = 4$, $N_H = 3$, and (c) wall 3 (18 g/min PMFR, no dwell, stop-start
 348 testing), $N_V = N_H = 4$. Because stress depends on cross-sectional area, and our area
 349 measurement introduced uncertainty, we have also plotted the mean of the extents of area-
 350 measurement-based uncertainty, propagated from caliper and micrometer uncertainty, in
 351 Figure 10 (computed similarly to how the “average” stress-strain curves themselves were
 352 computed). Data for some specimens were deemed to be unreliable (e.g. poor or failed DIC
 353 correlation, usually due to speckle pattern debonding) or simply missing due to operational
 354 challenges, and those specimens are excluded from the analysis. Recall that a stress-based
 355 criterion was used to determine when to scan. This means that there is some spread in

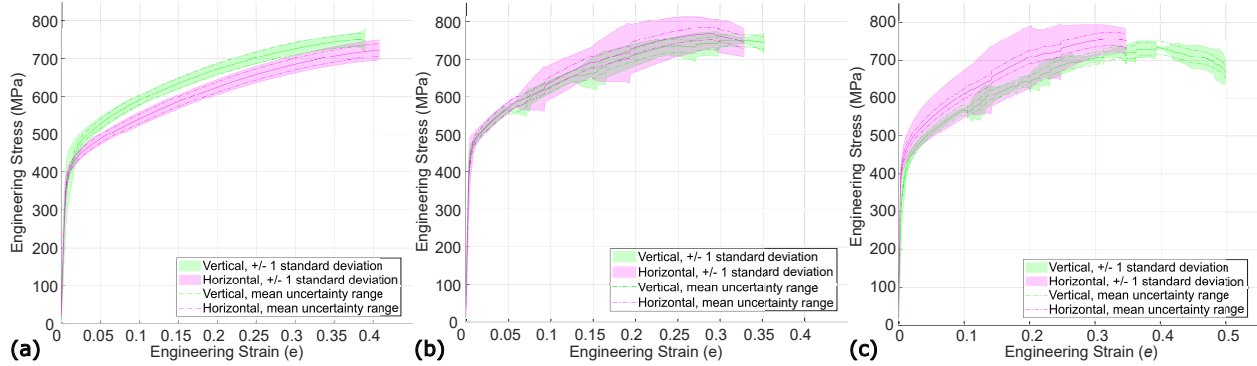


Figure 10: Averaged engineering stress-strain results for (a) wall 1, continuous testing, (b) wall 2 (60 s dwell), stop-start testing, (c) wall 3 (no dwell), stop-start. The light background is one standard deviation spread on the data, and the dot-dashed lines represent uncertainty in stress due to uncertainty in cross-sectional area measurement. This uncertainty was computed for each specimen: the differences between specimens are small and the mean uncertainty is shown. This figure highlights the variability between specimens and differences between H and V. Note: due to the specimen-to-specimen variability, the mean line does not represent any one specimen, but rather the general behavior of the set tested.

356 the strain values at which scans are taken. Thus, for wall 2 and wall 3, there are some
 357 points where the stress measured during loading and stress measured during hold periods
 358 are sometimes averaged together. This results in the increased variability and decreased
 359 smoothness of the averaged stress-strain response of walls 2 and 3 compared to wall 1. The
 360 curves in Figure 10 show that in general there are noticeable differences between orientations
 361 and between processing conditions. In wall 1, these differences are statistically significant
 362 throughout most of the stress-strain curve; walls 2 and 3 have somewhat artificially increased
 363 SDs, so are not statistically significant but this might be because of the added variability
 364 from averaging over the hold and non-hold periods as explained above. Also note that while
 365 a mean line is provided, this does not represent any particular specimen and is included to
 366 give a sense of the overall material performance and variability. Specific examples are given
 367 in 12. The full stress, strain, displacement, force and more is provided in the associated
 368 data publication, along with the techniques used to create these “average” representations
 369 [dataset] Kafka et al. (2022).

370 4.2. Horizontal versus vertical stress-strain response

371 To quantify the differences noted between H and V in the stress-strain curves above,
372 common parameters have been extracted from each. The commonly used single-point de-
373 scriptors of the stress-strain response elastic (Young's) modulus, 0.2% offset yield stress (σ_y),
374 ultimate tensile stress (UTS), and maximum measured elongation are used to make these
375 comparisons. Most mean values are within one standard deviation of the others, but some
376 trends seems to appear that may be of practical interest if not statistical significance. For
377 instance, in processing condition 1, horizontal specimens tend to have suppressed yield stress
378 and ultimate stress, but higher elastic moduli than their vertical counterparts. This does
379 not appear to be the case for the other processing conditions, but a more limited sample size
380 confounds the analysis somewhat; modulus is higher for horizontal specimens in processing
381 condition 3 compared to vertical specimens, but marginally lower in processing condition
382 2. Yield and ultimate stress appear broadly similar for horizontal and vertical specimens
383 in processing conditions 2 and 3, although horizontal is somewhat higher on average. Max-
384 imum elongation appears to be lower for the horizontal configuration across all processing
385 conditions, in keeping with the common trend that higher yield and ultimate stress often
386 correlate with lower elongation and toughness. Similar trends as observed here are noted
387 in the review of Hosseini *et al.* [Hosseini and Popovich \(2019\)](#), in particular higher elastic
388 modulus for horizontally oriented specimens compared to the vertical specimens. Further
389 details including box-and-whisker plots are given in [Appendix B](#).

390 The spread of results and relationship with location may be indicative of the impacts
391 of both microstructure and defects such as pores. However, fully developed necking occurs
392 and ductile response of the material appear to be relatively un-impacted by pores at the low
393 overall volume fraction observed in these samples, so this is unlikely to be a strong factor.
394 As an example, the distribution of pores and porosity for H3-4 and V3-4 are shown in Figure
395 [11](#). More recent work has also indicated that microstructure, rather than pores, is likely
396 dominant over pores for porosity levels as low as is observed here, cf. our results to those in

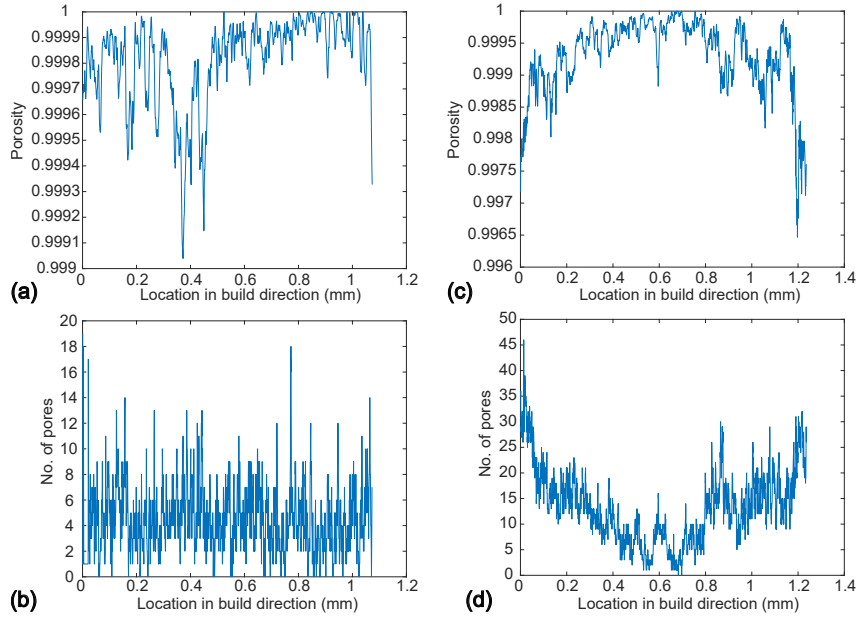


Figure 11: Plots of porosity (i.e., ratio of material to voids, $0 \leq x \leq 1$) and pore count (with smallest detectable pore about $2.197 \mu\text{m}^3$) versus height in the build direction computed on a slice-by-slice basis from the X-ray CT images. (a) H3-4 porosity, (b) H3-4 pore count, (c) V3-4 porosity, (d) V3-4 porosity. This indicates inhomogeneous distribution of porosity and pores throughout the build, although at relatively small amounts of both. Pore size analysis is shown later, in Section 4.4.2 and Appendix C.

397 [Watrung et al. \(2022\)](#), as an example of the scale of porosity required to govern response of
 398 AM IN718 (the comparison is imperfect, however, because [Watrung et al. \(2022\)](#) used laser
 399 powder bed fusion material with much smaller grain size).

400 These mechanical test data provide the context with which the following pore defor-
 401 mations can be more readily understood. Further plots are provided in the Supplemental
 402 Materials, showing the average stress-strain behavior and location dependency (Supplemen-
 403 tal Information 1 and Supplemental Information 2). The complete data are provided in the
 404 accompanying data publication [dataset] [Kafka et al. \(2022\)](#) for all specimens tested. For a
 405 more thorough analysis of thin-wall mechanical properties variations in the vertical config-
 406 uration and with different post-build heat treatments, similarly designed studies have been
 407 conducted and focus on relating thermal conditions to mechanical test results [Glerum et al.](#)
 408 [\(2021\)](#); [Bennett et al. \(2021, 2018\)](#).

409 4.3. Deformation observations

410 Stress-strain curves tested with the interrupted protocol for position 4 in walls 2 and
411 3 are given in Figure 12. For reference, a wrought IN718 test result for annealed material
412 (982 °C anneal, followed by air cooling according to the material supplier) using the same
413 specimen geometry and equipment is plotted as well. The heat treatments used for the
414 wrought and AM material are similar, though not identical. The surface roughness of the
415 wrought specimen was slightly higher, which may have driven earlier failure but is unlikely
416 to have increased stiffness and yield strength as dramatically as shown in Figure 12. In
417 both cases, precipitation strengthening during heat treatment is unlikely to have occurred,
418 although elemental segregation has been known to alter the heat treatment dynamics of AM
419 materials [Lass et al. \(2017\)](#). All the AM coupons are tougher than the wrought material,
420 with longer elongation but lower yield/ultimate stress and stiffness.

421 Two frames of deformation throughout the history of two specimens are given as an
422 example of the data collected during *in-situ* monitoring. These pores change shape during
423 the tension test, as shown in Figure 13; here, pores at the onset of plasticity and near failure
424 are shown, at the stress/strain points indicated by the corresponding number (1) through (4)
425 in Figure 12. Although comparing between surface and volumetric phenomena is imprecise
426 in these experiments, the equivalent 2D DIC strain maps recorded just prior to starting the
427 XCT scan for each of these four cases (H2-4 at 575 MPa and 700 MPa, and V3-4 at 575 MPa
428 and 650 MPa) are provided in Figure 14. Videos showing the deformation are provided in
429 Supplemental 4, and the complete datasets are provided in the associated data publication
430 [dataset] [Kafka et al. \(2022\)](#). Precise registration between the XCT volume and the DIC data
431 stream was not conducted. However, in general, the XCT images are slightly to viewer's right
432 of center in the gauge region in both cases, and can be qualitatively compared to the DIC.
433 From the DIC data, specimen V3-4 appears to undergo more uniform deformation, and once
434 necking occurs has a larger necked region compared to specimen H2-4. Likewise, necking can
435 be seen in the XCT images, although relating particular features is not possible. In images

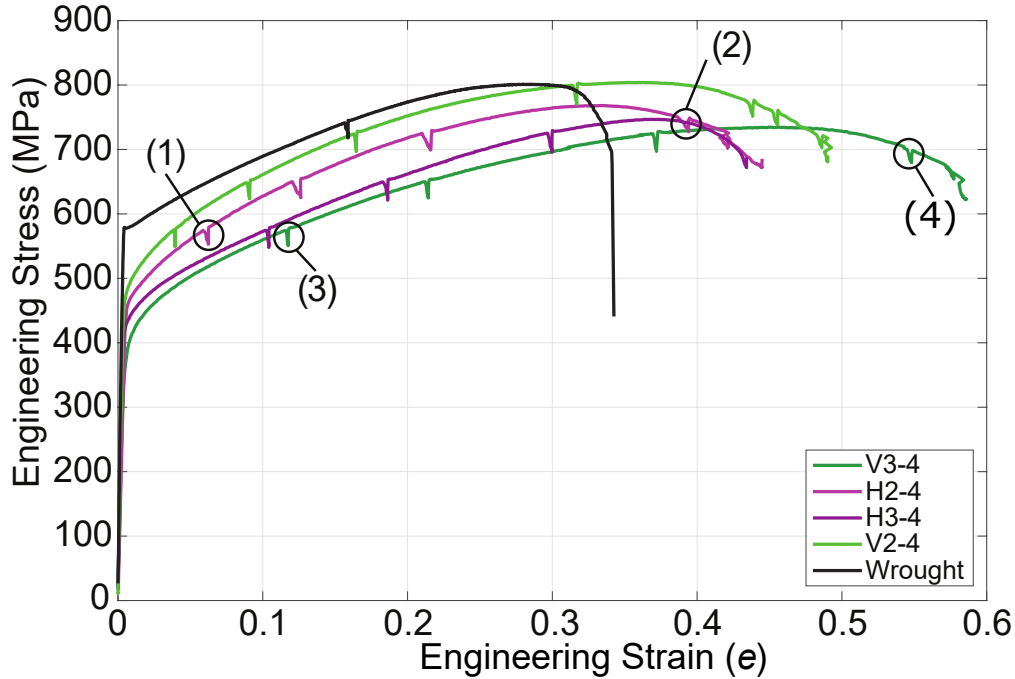


Figure 12: Stress-strain plot of four *in-situ* test specimens at location 4 in both vertical and horizontal configurations (V vs H) and walls 2 and 3. For reference they are compared to the behavior of a wrought, annealed IN718 specimen tested on the same equipment with the same specimen geometry (black line). Points called out on these curves correspond to the XCT scans shown in Figure 13

436 2 and 4, localize deformation has caused non-uniform stresses, i.e., the development of stress
 437 triaxiality, within the necked region. Previous literature has studied this effect, as the effects
 438 of stress triaxiality are important to understand the detailed progression of damage, e.g.,
 439 Weck et al. (2008); Landron et al. (2011); Maire et al. (2008). Future work focused on post-
 440 necking damage rather than the general progression of deformation might use these data to
 441 more thoroughly study the impact of triaxiality in void-based damage mechanics in DED
 442 IN718.

443 4.4. Defect tracking: observations and measurements

444 The primary use of XCT in this study is to track and measure pores as the metal de-
 445 forms. The information thus gathered can be used to better understand the deformation
 446 and failure mechanisms, and the roles that pores might have in these. Overall porosity was
 447 also computed from the XCT data and found to be less than 0.1%, and can be considered
 448 “fully dense” for AM materials.

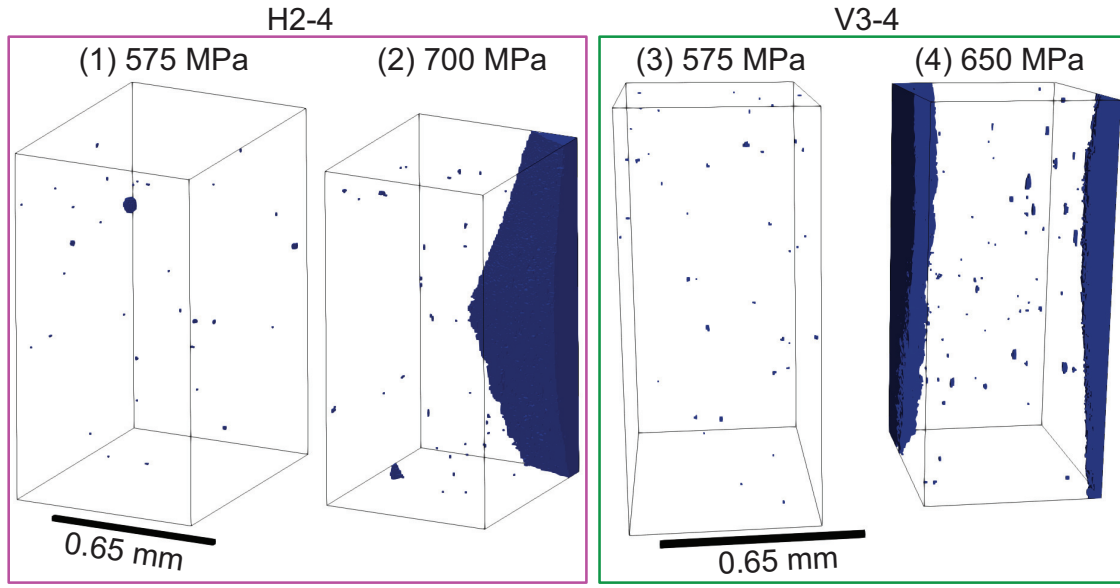


Figure 13: Two deformed configurations for specimens H2-4 and V3-4 (at the same relative position in each build), one at the onset of plasticity (left side) and the other at the final scan before failure (as indicated on the stress-strain curve in Figure 12 by the last drop in stress before failure). The large blue bands are the encroaching edges of the specimen as it thins during deformation. Notice that in the vertical configuration, where more elongation occurs, the pores have deformed substantially before failure but in the horizontal case similar pore evolution has not occurred, at least by visual inspection for this case.

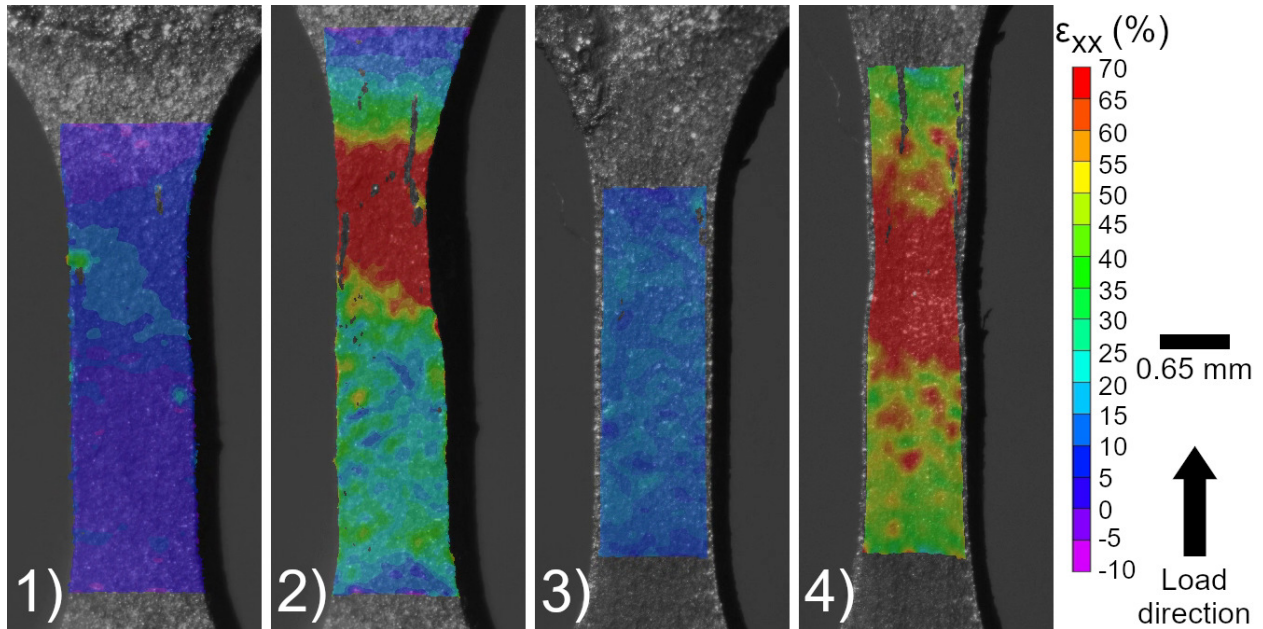


Figure 14: DIC surface strain maps showing deformation at two different load steps for two specimens (see also Supplemental 4); although individual strain concentrators are not possible to see, the same overall trend of uniform elongation followed by localization as expected and seen in the XCT images is observed. 1) H2-4 at 575 MPa applied engineering stress, 2) H2-4 at 700 MPa, 3) V3-4 at 575 MPa, and 4) V3-4 at 650 MPa. 1) through 4) correspond with the XCT images labeled (1) to (4) in Figure 13; XCT volumes are roughly 1.2 mm in height, located 0.15 mm below the end of the upper fillet.

449 4.4.1. *Single pore deformation*

450 The deformation progress of single pores throughout the strain-history can be tracked
451 in the XCT data, for example as shown in Figure 17, which demonstrates a series of four
452 subsequent pore states for a particularly large pore in specimen H1-8. XCT data was not
453 registered between data steps, and the field of view changed as the material deformed.
454 However, in the case, the pore stayed within the field of view throughout these four frames.
455 The stress-time points at which these snapshots were taken are circled in the stress-time
456 curve shown in Figure 16; the subset image shows the relative location of this pore of
457 interest within a sub-volume of the gauge region. Plotting stress versus time in Figure 16
458 emphasizes the creep region during the XCT scan. The stress trace also increases rapidly
459 from the post-creep value to the pre-stop value (within a couple of MPa generally) indicating
460 stress recovery upon continued displacement. This recovery can also be seen in the stress-
461 strain plot, e.g. Figure 12. Another, similar set of four snapshots during deformation is
462 provided in Figure 15, which shows a pore in specimen H2-4 undergoing a similar process.
463 These image for Figure 15 are rendered from spherical harmonic series expansion of the XCT
464 voxels providing a somewhat smoothed appearance. We propose that the plastic flow in a
465 single crystal results in the observed deformation in these cases. For large pores that are
466 easily isolated and tracked between scans, we observe that deformation causes the pore to
467 elongate in the direction of load, while narrowing in the other two orthogonal directions (see
468 Figures 15 and 17). This effect is quantified in Table 3, which confirms the observation,
469 and shows that length in the load direction (z-extent, as measured by an external bounding
470 box aligned along the image coordinates) increases while y-extent and x-extent decrease,
471 causing the pore to become more oblong as described by the L/T ratio increasing (where L
472 is the longest line that can be drawn through the pore and T is the shortest line orthogonal
473 to that). Overall, however, the pore tends to slightly increase in volume. In both cases,
474 narrowing is not necessarily consistent throughout the circumference, which is indicative of
475 the anisotropic nature of a single crystal in which the pore is likely embedded.

Table 3: H2-4 single pore geometry evolution. The pore in question can be seen in Figure 15, as well as in the upper-middle of Figure 13H2-4(1), however subsequent loading after 725 MPa moved this pore outside the field of view, as can be seen in Figure 13H2-4(2) taken after UTS (hence stress lower than 725 MPa). All lengths are in μm .

	0 MPa	575 MPa	650 MPa	725 MPa
x-extent	47	46	43	42
y-extent	49	50	45	44
z-extent	50	56	62	70
L/T	1.09	1.22	1.46	1.71
Volume (μm^3)	58 312	60 088	60 243	61 592

476 In general, this pore deformation is consistent with previous literature. For instance,
 477 Weck *et al.* Weck *et al.* (2008), found similar pore elongation for similar sized pores during
 478 deformation of pure copper and a copper-aluminum alloy. The density of pores in their
 479 work was specifically designed and observed to result in pore coalescence at higher levels of
 480 deformation, which was not observed at the porosity and pore spacing in the DED IN718
 481 tested here. However, the current work focuses more on overall deformation behavior than
 482 specifically on damage and failure and more detailed study may potentially make further
 483 progress in the damage of these materials.

484 4.4.2. Quantitative measurements of pore deformation

485 Observing a single pore deforming provides an indication of the general tendency of pores
 486 to elongate, but to generalize and compare between specimens we also analyzed the overall
 487 behavior of all detectable pores. Overall shape evolution statistics are given for four example
 488 specimens; the shape change in terms of the average lengths in x , y , and z are given in Figure
 489 18. This figure shows that the average pore behaves similarly to the individual large pores
 490 shown above. Pores on average tend to elongate in the direction of uniaxial loading (z),
 491 while contracting to a greater or lesser extent in the two orthogonal directions (x and y).
 492 The data in each graph in Figure 18 is an average over a minimum of 80 and a maximum
 493 of 390 pores. This is large enough of a data set to meaningfully construct averages, but
 494 also small enough that results may vary simply as different pores enter, or more commonly
 495 leave, the field of view of the XCT image as the specimen stretches and field of view changes

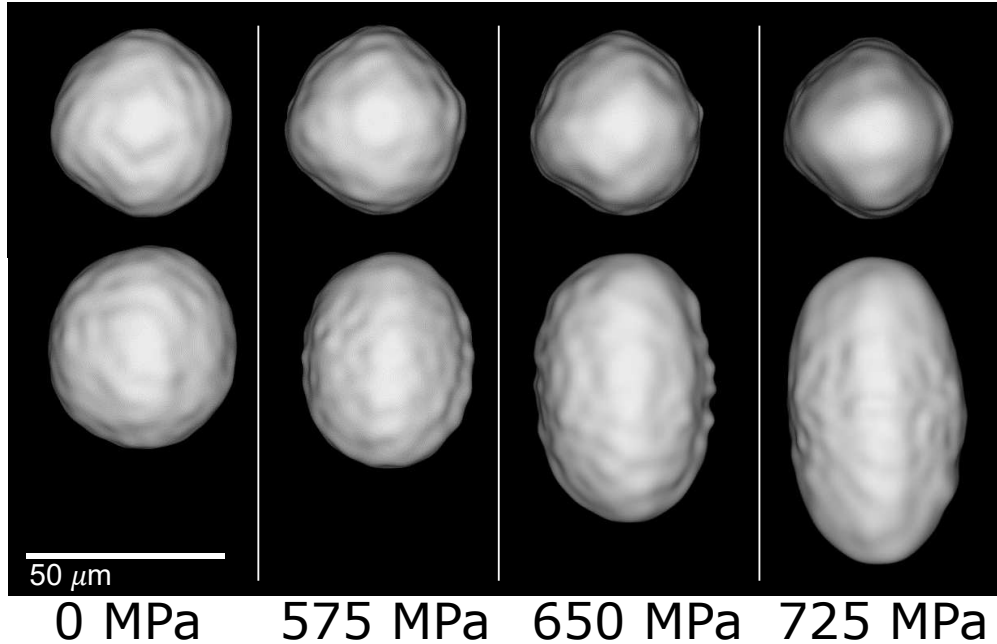


Figure 15: The large pore in H2-4, extending in the loading direction, before it moves out of the field of view. The prominent pore can be seen in context in Fig. 13(1) when at 575 MPa, visualized as smoothed renderings. Top row – looking down on the pore in the negative z-direction (into page). Bottom row – looking negative y-direction, z-direction is up, toward the top of the page.

496 slightly. The change in number of pores as a function of load level, shown in the tables in
 497 [Appendix C](#), represents this finite field of view effect. Hence some stress-level-to-stress-level
 498 variability within each specimen is expected.

499 One trend seems to be that the vertical specimens tend to undergo greater pore elon-
 500 gation, and experience an especially pronounced increase in elongation in the post-UTS
 501 (localization) region. Vertical specimens tend also towards greater elongation-to-failure, as
 502 noted in Section 4.2. This correlation may suggest that ductile mechanisms of deformation
 503 perhaps less closely spaced grain boundaries allowing for more free dislocation movement
 504 may involve greater pore shape change in the vertical configuration. These factors may
 505 also be related to anisotropy in the mechanical response observed above. Pores in the 60s
 506 dwell time wall (Wall 2) tend to undergo larger elongation as well, which may be related to
 507 differences in solidification cell structures that could develop differently because of different
 508 cooling rates and overall thermal conditions. In all cases, the volume of pores tend to in-
 509 crease with deformation, i.e. void growth, which is a commonly understood mechanism of

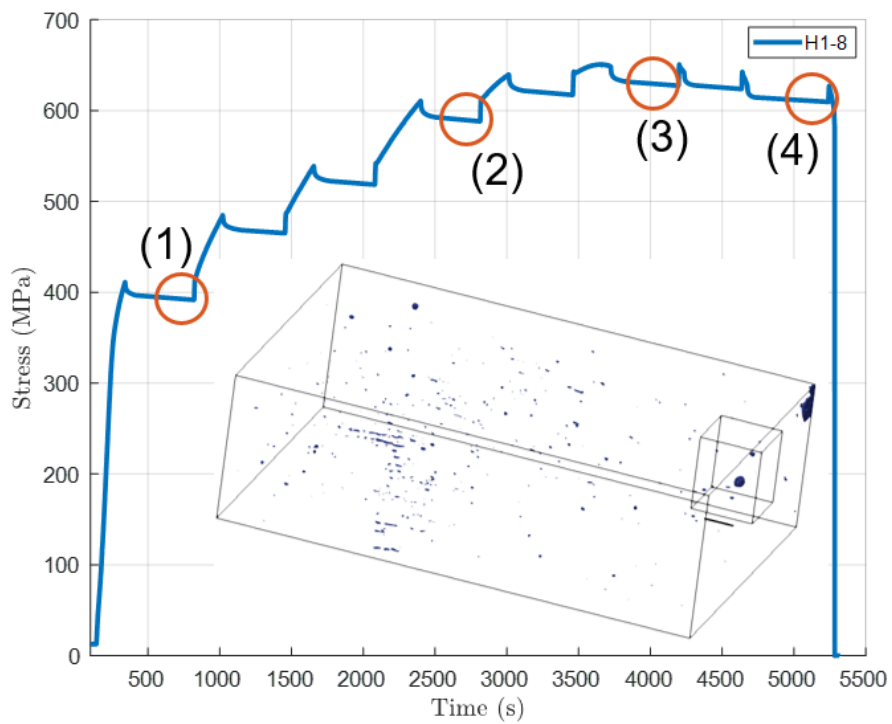


Figure 16: Stress versus time (which shows the hold periods), with the circled points showing stress values at which the single-pore deformation images shown in Figure 17 were taken. The single-pore deformation region in Figure 17 is a sub-volume of the larger image, highlighted by the smaller boxed region in the inset image.

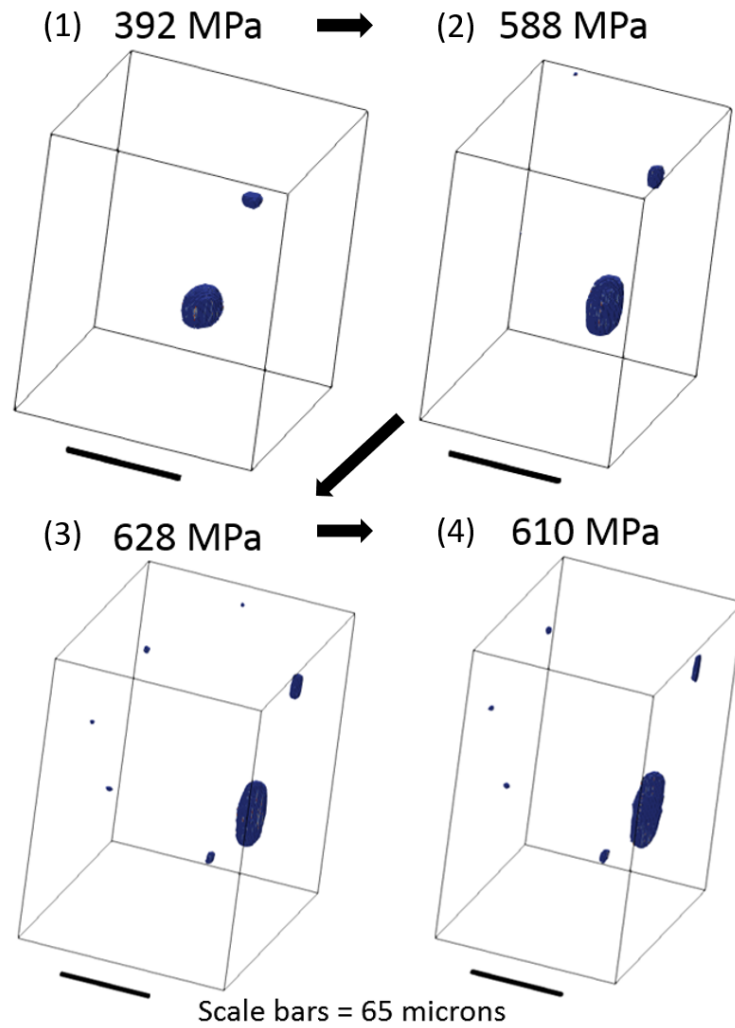


Figure 17: Images of a single, large pore deforming in specimen H1-8, along with the overall engineering stress state at which the respective images were taken; the pore elongates along the loading direction and new pores (either grown above the observation threshold, newly nucleated, or moved into the field of view) appear.

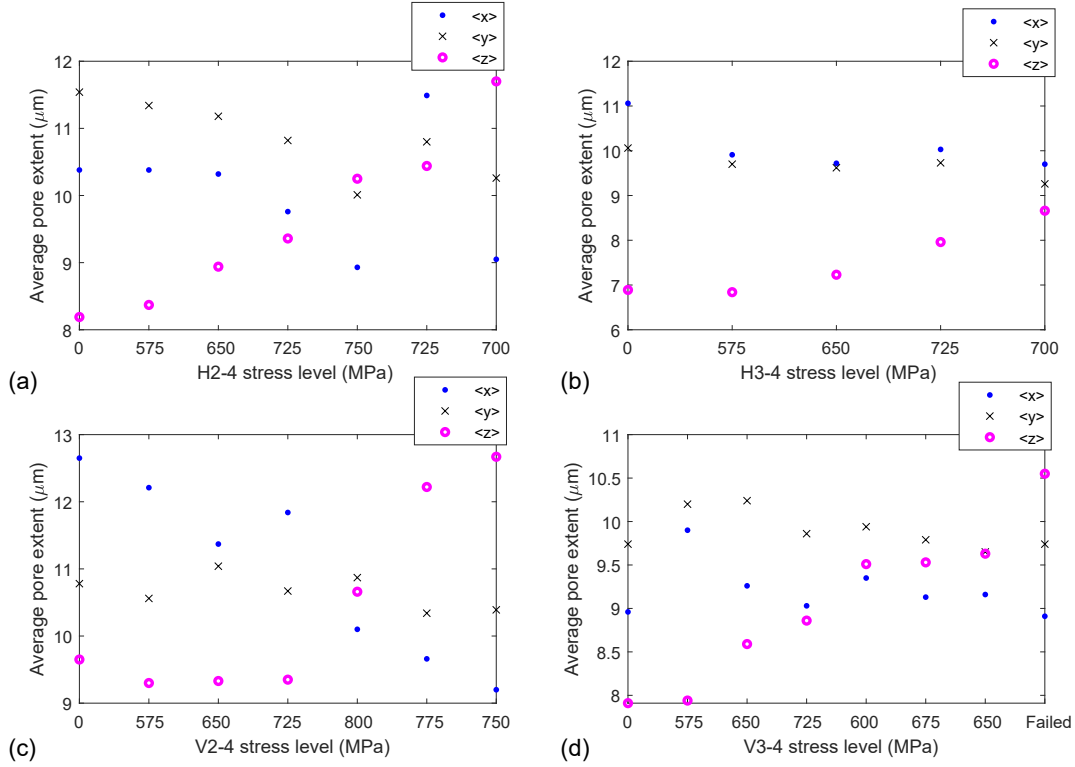


Figure 18: Pore extents (in μm) averaged across all pores in each subsequent XCT image during loading, for specimens: a) H2-4, b) H3-4, c) V2-4, d) V3-4.

510 ductile deformation.

511 The large pore shown in Figure 15 was approximately 10 times the volume of next biggest
 512 pore. This pore was not found in the other loading steps (i.e. it moved out of the field of
 513 view). The presence of this pore would skew the number-based averages of L , W , T , $\langle x \rangle$,
 514 $\langle y \rangle$, and $\langle z \rangle$. The average data for graphed in Figure 18 do not include this one big pore.
 515 Appendix C provides complete, detailed information regarding the average pore deformation
 516 in Tables C.5 (similarly, with the large pore removed for the first four entries), C.6, C.7, and
 517 C.8.

518 5. Crystal plasticity modeling of anisotropic pore evolution

519 The measurement of pore deformation shown here provides an opportunity to directly
 520 compare finite deformation microstructure-based modeling of pore deformation with exper-
 521 imental measurements. This provides increased confidence in the microscale models, if the

522 overall shape of the pore can be reproduced computationally when calibrating the model with
523 overall stress-strain data. The anisotropic pore deformation captured by the experiments
524 motivates using a crystal plasticity (CP) material law, derived from the work of McGinty
525 [McGinty \(2001\)](#).

526 Crystallographic measurements ([Appendix A](#)) show that the grains in this materials are
527 on the order of 2 mm tall (in the build direction) and 0.2 mm wide, i.e. much larger than the
528 pores. So it is reasonable to assume that a pore is entirely surrounded by a single crystal.
529 Thus, we build our model with a single crystal unit cell of $65 \mu\text{m} \times 65 \mu\text{m} \times 65 \mu\text{m}$ embedded
530 with a relatively large pore. The pore itself was extracted directly from the XCT images
531 ([Figure 19](#)), and thus the initial shape of the pore is identical in experiment and simulation.

532 The assumption of a single crystal surrounding the pore also provides a means with
533 which to conduct inverse modeling: the crystallographic orientation surrounding pore pre-
534 dominantly impacts the orientation of maximal and minimal contraction of the pore during
535 deformation, and this local information can be used to identify grain orientation (as a model
536 input) while keeping all calibration parameters constant. Although with the current dataset
537 we are unable to validate the orientation prediction, we can at least demonstrate this kind
538 of potential usage for coupled simulation-experimental investigations, with the hope it could
539 be proven useful in future investigations.

540 Details of the CP material model implementation are provided in [Appendix D](#). The
541 CP material model was implemented in a reduced order modeling method called Crystal
542 Plasticity Self-consistent Clustering Analysis (CPSCA) [Yu et al. \(2019\)](#); [Liu et al. \(2018\)](#).
543 The finite deformation implementation of CPSCA used for this work is explained in detail in
544 [Yu \(2019\)](#). The material parameters, given in [Table 4](#), are used to approximately match the
545 average stress-strain curves. Currently, the elastic properties are isotropic, not anisotropic,
546 which had little impact upon the overall results.

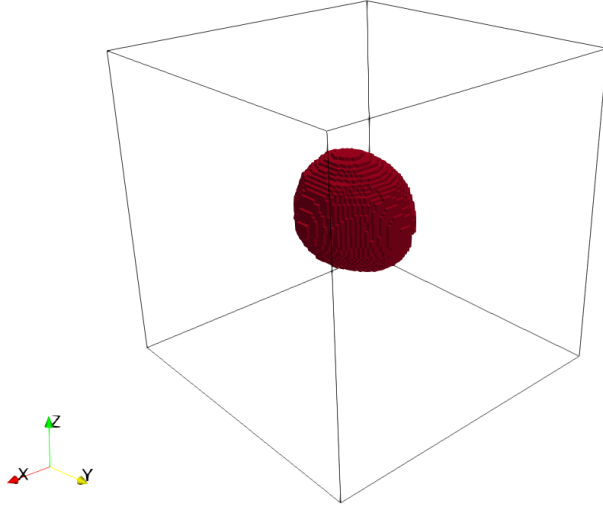


Figure 19: A single crystal unit cell of $65\ \mu\text{m} \times 65\ \mu\text{m} \times 65\ \mu\text{m}$ embedded with a big pore (in red).

Table 4: Crystal plasticity parameters, those marked with a dagger symbol were taken directly from [Cruzado et al. \(2017\)](#). The remainder were calibrated with the thin wall tensile test data.

C_{11} (GPa)	C_{12} (GPa)	C_{44} (GPa)	
196.40	84.17	56.12	
$\dot{\gamma}_0^\alpha$ (s^{-1})	\tilde{m}	$\tau_0^{\alpha,t=0}$ (MPa)	$a^{\alpha,t=0}$ (MPa)
2.42×10^{-3} †	58.8 †	171.85	0.0
H (MPa)	R (MPa)	h (MPa)	r (MPa)
1.0	0.0	500.0	0.0

547 With these parameters calibrated, the remaining question is: what grain orientation led
548 to the specific pore deformation observed in the experiment? To answer this question, an
549 optimization algorithm is used to iteratively find the grain orientation by minimizing the
550 difference between the predicted pore shape and measured pore shape, using of a fast nu-
551 merical model. This process only changed the input grain orientation, none of the calibration
552 parameters.

553 5.1. Overall CPSCA pore shape predictions

554 Because the pore is in a single crystal, preferential deformation in one orientation occurs
555 driving the initially sphere-like defect to a three-axis ellipsoid. The overall shape of the
556 pore throughout the load steps matches between the prediction of the simulation and the
557 measurement of the experiment. By changing the orientation of the crystal in the model,
558 the observed axes of minimal and maximal contraction can be reproduced. Other than
559 the orientation of the maximal and minimal constrictions, the overall shape prediction is
560 independent of the inverse model described above. Although only shown for one case, the
561 high quality of the match provide some confidence in the ability of our CP method to
562 reproduce the local deformation of micro-scale pores in DED IN718, but further validation
563 would be beneficial. A comparison of two projections (top-down and side-on) of the pore as
564 measured and as modeled are shown in Figure 20. In both simulation and experiment, the
565 pore extends in the load direction as shown in the side projection in the top two rows of
566 Figure 20. The pore predominately contracts in the 45° direction in the x-y plane while hardly
567 contracting at all in the 135° direction in the x-y plane, as shown in the top-down projection
568 in the second two rows of Figure 20. These deformations result are from a crystal with
569 lattice orientation $(45^\circ, 45^\circ, 0^\circ)$. Only the input parameter of grain orientation was changed,
570 the calibration parameters were unmodified, to identify the grain orientation that resulted
571 in a good match in deformation. Thus, we suppose that a) the initial calibration could
572 produce the given void deformation as a pure prediction, given grain orientation information
573 (unavailable with the current experiment); and b) that the grain orientation can be computed
574 using an inverse approach and CP model calibrated to average stress-strain properties.

575 6. Summary, Conclusions, and Future Work

576 6.1. Summary and Conclusions

577 This work presented a series of pore and mechanical characterizations of thin-wall IN718
578 samples produced using DED, and tested with *in-situ* techniques to track pores during

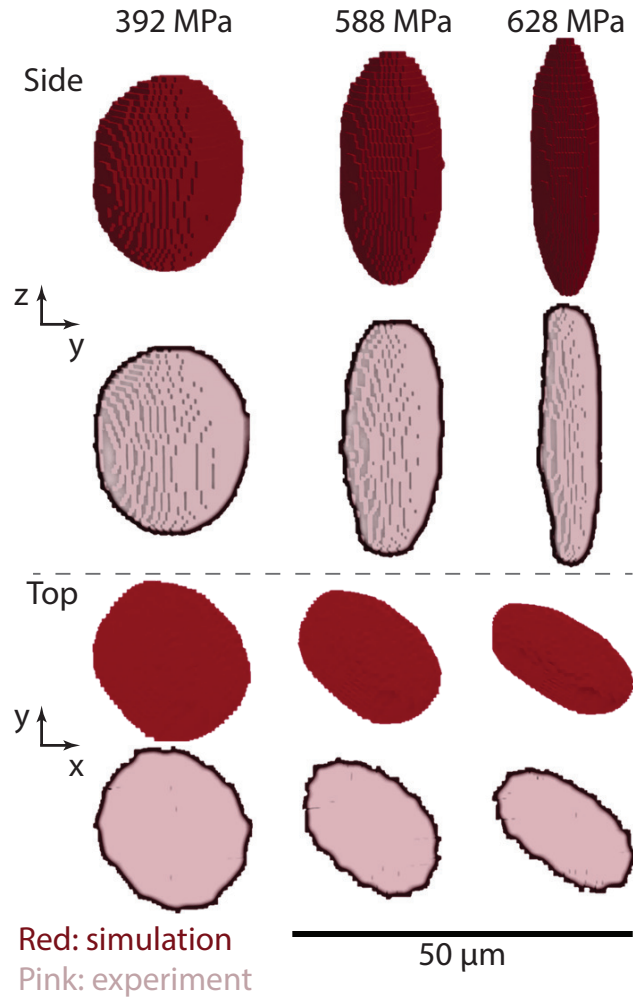


Figure 20: A single pore deforming in a single crystal. The two rows show “side” and “top” views, with each sub-row showing the comparison of measurement (red) and model (pink) at different stress levels. The model predicts well the deformation patterns observed in the experiment using macroscopically calibrated model parameters and a lattice orientation of $(45^\circ, 45^\circ, 0^\circ)$.

579 mechanical testing. Largely 3D measurements showed the complex, heterogeneous, and
580 anisotropic nature of the material. Mechanical testing alongside 3D measurements of pores
581 provided unique insight into the deformation behavior of the material in ways that would
582 not be possible to understand without *in-situ* monitoring of deformation. In summary:

- 583 • Material properties vary significantly from location to location, with orientation, and
584 with processing condition. Orientation variability is in keeping with prior published
585 results for similar material. Although a wide spread was observed in our tests, the
586 general trends indicated that horizontally oriented specimens have similar higher elastic
587 modulus, yield and ultimate stress at the deficit of elongation when compared with
588 vertically oriented specimens.
- 589 • We hypothesize that location-to-location differences are related to thermal difference
590 in the build; although differences in porosity exist, at the scales of pores observed,
591 they seem to have little impact on the progression of plastic deformation, necking, and
592 ductile damage.
- 593 • The wall with 60s dwell time seems to generally undergo large deformation before
594 failure; prior work also indicates that local thermal condition difference lead to quan-
595 tifiable differences in UTS, [Bennett et al. \(2018\)](#), although this was not directly studied
596 in the current work.
- 597 • Pore deformation has been measured:
 - 598 – For this process and material, pores are on the sub-grain scale (grains are relatively
599 large compared to pores); for the larger pores specifically studied, pore volume
600 tends to increase slightly as deformation level increases.
 - 601 – Pores tend to elongate with the material during deformation.
 - 602 – Greater pore shape change appears to correlate with greater maximum elongation,
603 i.e., the build with 60s dwell (wall 2) tended to undergo more elongation and

604 greater shape change than those in the walls without a dwell time.

- 605 – In most cases, these failures do not seem strongly defect-driven and ductile deformation develops despite a general dispersion of small, generally spherical pores.
606 We conclude that for ligaments on the 1 mm-edge-length scale such as our test
607 specimens, pores with average size roughly $10\ \mu\text{m}$ are not dominating the plastic
608 response.
609

- 610 • A crystal plasticity material model implemented in the CPSCA reduced order scheme
611 was used to simulate the pore shape change of a specific, large pore.
- 612 • Although not validated, one potential implication of the CPSCA modeling is that grain
613 orientation might be inferred from preferential single-crystal deformation patterns

614 These conclusions are general restricted to similar material, i.e. high-density IN718 with
615 small, semi-randomly distributed, roughly spherical pores. Only highlights of the complete
616 data set obtained have been shown, along with aggregated data. Full testing to construct
617 the average stress-strain curves included some 74 in-situ tests. This full data set represents
618 a rich corpus of evidence that could be further explored in several different ways in future
619 work.

620 The full data set, including stress-strain data (and curves), selected XCT data, and
621 Matlab processing scripts are provided, archived and publicly accessible by DOI on NIST's
622 MIDAS data service (URL/DOI to be added). Interested readers, and those curious enough
623 to pursue future work with the data are encouraged to contact us and download the publicly
624 available dataset.

625 *6.2. Possible future work*

626 In order to make the most use of the *in-situ* testing, digital volume correlation (DVC) or a
627 similar technique, could be used to reconstruct 3D strain fields in the measured volume. This
628 would allow for even more direct comparison between models and experiments. It would also

629 provide a deeper insight into the deformation behaviors of the material. However, because
630 the only contrast available currently in these specimens is the pores themselves, it is unlikely
631 that information on the pore scale or in between pores could be reliably obtained with the
632 current data.

633 Further it is well known that localized deformation (necking) will change the stress tri-
634 axiality within the area-reduction region. Since stress triaxiality is a controlling factor in
635 damage and fracture, a future study focused on post-localization deformation and fracture
636 behavior could use this data to compute area reduction, ductility, and localize triaxiality
637 changes; computation of the triaxiality from these images would be relatively easy. The
638 addition of optical or electron microscopy fractography or other post-failure analysis would
639 be of interest to more thoroughly quantify the failure behavior and any potential differences
640 in failure behavior between build conditions and conventionally processed IN718.

641 Further analysis of microstructure features other than pores could be conducted. Study
642 of the reduction of area versus elongation would provide a quantifiable measure for ductility.
643 Measurement of final cross section could be done on either the specimens themselves, or using
644 reconstructed XCT scans of the fracture regions (Supplemental Information 3 provides an
645 example of the XCT scans of fracture regions). Noisy thermal measurements made during
646 the build make it difficult to quantify the thermal conditions and thus difficult to relate
647 those to specific specimens and their behavior. However, it has been possible to compare
648 ultimate tensile strength to thermal indicators for these specimens ([Bennett et al. \(2018\)](#)),
649 and future analysis could include more thorough comparisons between measured mechanical
650 performance indicators (e.g. stiffness, ultimate strength, yield strength, elongation) and
651 spatial location or thermal history for the various different coupons and walls. Another
652 recent study on the same material found a correlation between solidification cooling rate
653 and pore size [Kafka et al. \(2021\)](#), and further correlations between thermal indicators and
654 critical features for modeling would be advantageous to discover.

655 Another aspect that could be further studied is the systematization of inverse modeling

656 to identify grain orientation on the basis of pore deformation. In theory, such a model could
657 be used to provide grain orientation maps, where orientation is known in the local vicinity of
658 an observed pore. While computationally somewhat expensive, this would provide additional
659 information to XCT-only experiments (i.e. no diffraction data is collected) with little or no
660 additional experimental effort. This would enrich the kind of data that can be collected, in
661 3D, on tomographic equipment, possibly even on laboratory-scale *in-situ* XCT equipment.

662 **Authors' Contributions (CRediT)**

663 **Orion L. Kafka:** Conceptualization, methodology, software, validation, investigation, re-
664 sources, data curation, writing – original draft, writing – review & editing, project adminis-
665 tration, visualization, supervision, funding acquisition.

666 **Cheng Yu:** Conceptualization, methodology, software, validation, investigation, writing –
667 review & editing, visualization, funding acquisition.

668 **Puikui Cheng:** Conceptualization, methodology, investigation, writing – review & editing,
669 project administration, funding acquisition.

670 **Sarah Wolff:** Conceptualization, methodology, investigation, resources, writing – review &
671 editing, project administration, funding acquisition.

672 **Jennifer Bennett:** Conceptualization, methodology, investigation, writing – review & edit-
673 ing.

674 **Edward Garboczi:** Investigation, software, supervision, writing – review & editing.

675 **Jian Cao:** Resources, funding acquisition, writing–review & editing.

676 **Xianghui Xiao:** Conceptualization, methodology, software, resources, writing–review &
677 editing.

678 **Wing Kam Liu:** Resources, supervision, funding acquisition, writing–review & editing.

679 **7. Acknowledgments**

680 This work made use of the MatCI Facility which receives support from the MRSEC
681 Program (National Science Foundation DMR-1720139) of the Materials Research Center
682 at Northwestern University. We specifically thank Carla Shute at the MatCI facility for
683 her advice during specimen preparation. Specimens were fabricated using funding from
684 DMDII grant number 15-07-07; OLK, CY, and WKL thank the National Science Foundation
685 for support under grants CMMI-1762035 and CMMI-1934367. Part of this research was
686 conducted while OLK held a National Research Council Postdoctoral Research Associateship
687 at the National Institute of Standards and Technology. We gratefully acknowledge the help of
688 J.-S. Park of APS Beamline 11D, who provided the mini-tensile load frame used throughout
689 the work, as well as technical support for the load frame and helpful suggestions for the
690 research.

691 **8. Declaration of Competing Interests**

692 The authors declare that they have no known competing financial interests or personal
693 relationships that could have appeared to influence the work reported in this paper.

694 **9. Data Availability**

695 All raw data used for this work, and processed data that appears in the manuscript is
696 made available in the associated data publication [dataset] [Kafka et al. \(2022\)](#). Further
697 processed data is available upon reasonable request.

698 **References**

699 Anderson, M., Thielin, A.L., Bridier, F., Bocher, P., Savoie, J., 2017. δ Phase precipitation
700 in Inconel 718 and associated mechanical properties. *Mater. Sci. Eng, A* 679, 48 – 55.
701 [doi:10.1016/j.msea.2016.09.114](https://doi.org/10.1016/j.msea.2016.09.114).

702 Bain, E.D., Garboczi, E.J., Seppala, J.E., Parker, T.C., Migler, K.B., 2019. AMB2018-
703 04: Benchmark Physical Property Measurements for Powder Bed Fusion Additive Man-
704 ufacturing of Polyamide 12. *Integr. Mater. Manuf. Innov.* 8, 335–361. doi:[10.1007/
705 s40192-019-00146-3](https://doi.org/10.1007/s40192-019-00146-3).

706 Bennett, J., Glerum, J., Cao, J., 2021. Relating additively manufactured part tensile prop-
707 erties to thermal metrics. *CIRP Annals* 70, 187–190. doi:[10.1016/j.cirp.2021.04.053](https://doi.org/10.1016/j.cirp.2021.04.053).

708 Bennett, J.L., Kafka, O.L., Liao, H., Wolff, S.J., Yu, C., Cheng, P., Hyatt, G., Ehmann, K.,
709 Cao, J., 2018. Cooling rate effect on tensile strength of laser deposited Inconel 718, in:
710 *Procedia Manuf.*, pp. 912–919. doi:[10.1016/j.promfg.2018.07.118](https://doi.org/10.1016/j.promfg.2018.07.118).

711 Bennett, J.L., Wolff, S.J., Hyatt, G., Ehmann, K., Cao, J., 2017. Thermal effect on clad
712 dimension for laser deposited Inconel 718. *J. Manuf. Processes* 28, 550 – 557. doi:[10.
713 1016/j.jmapro.2017.04.024](https://doi.org/10.1016/j.jmapro.2017.04.024).

714 Benzing, J.T., Liew, L.A., Hrabe, N., DelRio, F.W., 2020. Tracking Defects and Microstruc-
715 tural Heterogeneities in Meso-Scale Tensile Specimens Excised from Additively Manufac-
716 tured Parts. *Exp. Mech.* 60, 165–170. doi:[10.1007/s11340-019-00558-4](https://doi.org/10.1007/s11340-019-00558-4).

717 Bigger, R., Blaysat, B., Boo, C., Grewer, M., Hu, J., Jones, A., Klein, M., Raghavan, K.,
718 Reu, P., Schmidt, T., Siebert, T., Simenson, M., Turner, D., Vieira, A., Weikert, T., 2018.
719 A Good Practices Guide for Digital Image Correlation. *Int. Digital Image Correl. Soc.* ,
720 94doi:[10.32720/idics/gpg.ed1](https://doi.org/10.32720/idics/gpg.ed1).

721 Blackwell, P., 2005. The mechanical and microstructural characteristics of laser-deposited
722 IN718. *J. Mater. Process. Technol.* 170, 240 – 246. doi:[10.1016/j.jmatprotec.2005.05.
723 005](https://doi.org/10.1016/j.jmatprotec.2005.05.005).

724 Burhenne, S., Jacob, D., Henze, G.P., 2011. Sampling based on Sobol sequences for Monte
725 Carlo techniques applied to building simulations. *Proceedings of Building Simulation*

726 2011: 12th Conference of International Building Performance Simulation Association ,
727 1816–1823.

728 Carlton, H.D., Haboub, A., Gallegos, G.F., Parkinson, D.Y., MacDowell, A.A., 2016. Dam-
729 age evolution and failure mechanisms in additively manufactured stainless steel. *Mater.*
730 *Sci. Eng. A* 651, 406–414. doi:[10.1016/j.msea.2015.10.073](https://doi.org/10.1016/j.msea.2015.10.073).

731 Cruzado, A., LLorca, J., Segurado, J., 2017. Modeling cyclic deformation of Inconel 718
732 superalloy by means of crystal plasticity and computational homogenization. *Int. J. Solids*
733 *Struct.* 122, 148–161.

734 Efstathiou, C., Boyce, D., Park, J.S., Lienert, U., Dawson, P., Miller, M., 2010. A method for
735 measuring single-crystal elastic moduli using high-energy X-ray diffraction and a crystal-
736 based finite element model. *Acta Mater.* 58, 5806 – 5819. doi:[10.1016/j.actamat.2010.](https://doi.org/10.1016/j.actamat.2010.06.056)
737 [06.056](https://doi.org/10.1016/j.actamat.2010.06.056).

738 Gan, Z., Li, H., Wolff, S.J., Bennett, J.L., Hyatt, G., Wagner, G.J., Cao, J., Liu, W.K., 2019.
739 Data-driven microstructure and microhardness design in additive manufacturing using a
740 self-organizing map. *Engineering* 5, 730 – 735. doi:[10.1016/j.eng.2019.03.014](https://doi.org/10.1016/j.eng.2019.03.014).

741 Garboczi, E.J., Hrabe, N., 2020a. Particle shape and size analysis for metal powders used
742 for additive manufacturing: Technique description and application to two gas-atomized
743 and plasma-atomized Ti64 powders. *Addit. Manuf.* 31, 100965. doi:[10.1016/j.addma.](https://doi.org/10.1016/j.addma.2019.100965)
744 [2019.100965](https://doi.org/10.1016/j.addma.2019.100965).

745 Garboczi, E.J., Hrabe, N., 2020b. Three-Dimensional Particle Shape Analysis Using X-
746 ray Computed Tomography: Experimental Procedure and Analysis Algorithms for Metal
747 Powders. *J. Visualized Exp.* doi:[10.3791/61636](https://doi.org/10.3791/61636).

748 Glerum, J., Bennett, J., Ehmann, K., Cao, J., 2021. Mechanical properties of hybrid addi-
749 tively manufactured Inconel 718 parts created via thermal control after secondary treat-

750 ment processes. *J. Mater. Process. Technol.* 291, 117047. doi:[10.1016/j.jmatprotec.](https://doi.org/10.1016/j.jmatprotec.2021.117047)
751 [2021.117047](https://doi.org/10.1016/j.jmatprotec.2021.117047).

752 Gordon, J., Vinci, R., Hochhalter, J., Rollett, A., Harlow], D.G., 2019. Quantification of
753 location-dependence in a large-scale additively manufactured build through experiments
754 and micromechanical modeling. *Materialia* 7, 100397. doi:[10.1016/j.mtla.2019.100397](https://doi.org/10.1016/j.mtla.2019.100397).

755 Gorelik, M., 2017. Additive manufacturing in the context of structural integrity. *Int. J.*
756 *Fatigue* 94, 168–177. doi:[10.1016/j.ijfatigue.2016.07.005](https://doi.org/10.1016/j.ijfatigue.2016.07.005).

757 Gürsoy, D.D., De Carlo, F., Xiao, X., Jacobsen, C., 2014. TomoPy: a framework for the
758 analysis of synchrotron tomographic data. *J. Synchrotron Radiat.* 21, 1188–1193. doi:[10.](https://doi.org/10.1107/S1600577514013939)
759 [1107/S1600577514013939](https://doi.org/10.1107/S1600577514013939).

760 Guévenoux, C., Hallais, S., Charles, A., Charkaluk, E., Constantinescu, A., 2020. Influence
761 of interlayer dwell time on the microstructure of Inconel 718 laser clad components.
762 *Opt. Laser Technol.* 128, 106218. doi:[10.1016/j.optlastec.2020.106218](https://doi.org/10.1016/j.optlastec.2020.106218).

763 Hastie, J.C., Koelblin, J., Kartal, M.E., Attallah, M.M., Martinez, R., 2021. Evolution of
764 internal pores within AlSi10Mg manufactured by laser powder bed fusion under tension:
765 As-built and heat treated conditions. *Mater. Des.* 204, 109645. doi:[10.1016/j.matdes.](https://doi.org/10.1016/j.matdes.2021.109645)
766 [2021.109645](https://doi.org/10.1016/j.matdes.2021.109645).

767 Herroitt, C., Li, X., Kouraytem, N., Tari, V., Tan, W., Anglin, B., Rollett, A., Spear, A.,
768 2019. A multi-scale, multi-physics modeling framework to predict spatial variation of
769 properties in additive-manufactured metals. *Model. Simul. Mater. Sci. Eng.* 27, 025009.
770 doi:[10.1088/1361-651x/aaf753](https://doi.org/10.1088/1361-651x/aaf753).

771 Hosseini, E., Popovich, V., 2019. A review of mechanical properties of additively manufac-
772 tured Inconel 718. *Addit. Manuf.* 30, 100877. doi:[10.1016/j.addma.2019.100877](https://doi.org/10.1016/j.addma.2019.100877).

773 Jinoop, A., Paul, C., Mishra, S., Bindra, K., 2019. Laser Additive Manufacturing using di-
774 rected energy deposition of Inconel-718 wall structures with tailored characteristics. Vac-
775 uum 166, 270 – 278. doi:[10.1016/j.vacuum.2019.05.027](https://doi.org/10.1016/j.vacuum.2019.05.027).

776 Kafka, O.L., Jones, K.K., Yu, C., Cheng, P., Liu, W.K., 2021. Image-based multiscale
777 modeling with spatially varying microstructures from experiments: Demonstration with
778 additively manufactured metal in fatigue and fracture. J. Mech. Phys. Solids 150. doi:[10.1016/j.jmps.2021.104350](https://doi.org/10.1016/j.jmps.2021.104350).

780 Kafka, O.L., Yu, C., Cheng, P., Wolff, S.J., Bennett, J.L., Garboczi, E., Cao, J., Xiao,
781 X., Liu, W.K., 2022. X-ray computed tomography analysis of pore deformation in IN718
782 made with directed energy deposition via in-situ tensile testing. URL: <https://data.nist.gov/od/id/mds2-2512>, doi:[doi:10.18434/mds2-2512](https://doi.org/10.18434/mds2-2512).

784 Kim, F.H., Moylan, S.P., Phan, T.Q., Garboczi, E.J., 2020. Investigation of the Effect
785 of Artificial Internal Defects on the Tensile Behavior of Laser Powder Bed Fusion 17–4
786 Stainless Steel Samples: Simultaneous Tensile Testing and X-Ray Computed Tomography.
787 Exp. Mech. 60, 987–1004. doi:[10.1007/s11340-020-00604-6](https://doi.org/10.1007/s11340-020-00604-6).

788 Krakhmalev, P., Fredriksson, G., Yadroitsava, I., Kazantseva, N., du Plessis, A., Yadroit-
789 sev, I., 2016. Deformation Behavior and Microstructure of Ti6Al4V Manufactured by
790 SLM. Phys. Procedia 83, 778–788. doi:[10.1016/j.phpro.2016.08.080](https://doi.org/10.1016/j.phpro.2016.08.080). laser Assisted
791 Net Shape Engineering 9 International Conference on Photonic Technologies Proceedings
792 of the LANE 2016 September 19-22, 2016 Fürth, Germany.

793 Kruth, J.P., Vandenbroucke, B., Van Vaerenbergh, J., Naert, I., 2005. Rapid manufacturing
794 of dental prostheses by means of selective laser sintering/melting. Proc. AFPR S 4, 176–
795 186.

796 Lambarri, J., Leunda, J., Navas], V.G., Soriano, C., Sanz, C., 2013. Microstructural and

797 tensile characterization of Inconel 718 laser coatings for aeronautic components. Opt.
798 Lasers Eng. 51, 813 – 821. doi:[10.1016/j.optlaseng.2013.01.011](https://doi.org/10.1016/j.optlaseng.2013.01.011).

799 Landron, C., Maire, E., Bouaziz, O., Adrien, J., Lecarme, L., Bareggi, A., 2011. Validation
800 of void growth models using x-ray microtomography characterization of damage in dual
801 phase steels. Acta Materialia 59, 7564–7573. doi:[https://doi.org/10.1016/j.actamat.](https://doi.org/10.1016/j.actamat.2011.08.046)
802 [2011.08.046](https://doi.org/10.1016/j.actamat.2011.08.046).

803 Lass, E.A., Stoudt, M.R., Williams, M.E., Katz, M.B., Levine, L.E., Phan, T.Q., Gnaeupel-
804 Herold, T.H., Ng, D.S., 2017. Formation of the Ni₃Nb δ -Phase in Stress-Relieved Inconel
805 625 Produced via Laser Powder-Bed Fusion Additive Manufacturing. Metall. Mater. Trans.
806 A 48, 5547–5558. doi:[10.1007/s11661-017-4304-6](https://doi.org/10.1007/s11661-017-4304-6).

807 Lecarme, L., Maire, E., Kumar, A., De Vleeschouwer, C., Jacques, L., Simar, A., Pardoën,
808 T., 2014. Heterogenous void growth revealed by in situ 3-D X-ray microtomography using
809 automatic cavity tracking. Acta Mater. 63, 130–139. doi:[10.1016/j.actamat.2013.10.](https://doi.org/10.1016/j.actamat.2013.10.014)
810 [014](https://doi.org/10.1016/j.actamat.2013.10.014).

811 LePage, W.S., Daly, S.H., Shaw, J.A., 2016. Cross Polarization for Improved Digital Image
812 Correlation. Exp. Mech. 56, 969–985. doi:[10.1007/s11340-016-0129-2](https://doi.org/10.1007/s11340-016-0129-2).

813 Li, X., Liu, Z., Cui, S., Luo, C., Li, C., Zhuang, Z., 2019. Predicting the effective mechanical
814 property of heterogeneous materials by image based modeling and deep learning. Comp.
815 Methods Appl. Mech. Eng. 347, 735–753. doi:[10.1016/J.CMA.2019.01.005](https://doi.org/10.1016/J.CMA.2019.01.005).

816 Li, Z., Chen, J., Sui, S., Zhong, C., Lu, X., Lin, X., 2020. The microstructure evolution and
817 tensile properties of Inconel 718 fabricated by high-deposition-rate laser directed energy
818 deposition. Addit. Manuf. 31, 100941. doi:[10.1016/j.addma.2019.100941](https://doi.org/10.1016/j.addma.2019.100941).

819 Limodin, N., Réthoré, J., Buffière, J.Y., Hild, F., Roux, S., Ludwig, W., Rannou, J.,
820 Gravoil, A., 2010. Influence of closure on the 3D propagation of fatigue cracks in a

821 nodular cast iron investigated by X-ray tomography and 3D volume correlation. *Acta*
822 *Mater.* 58, 2957–2967. doi:[10.1016/j.actamat.2010.01.024](https://doi.org/10.1016/j.actamat.2010.01.024).

823 Liu, F., Lin, X., Huang, C., Song, M., Yang, G., Chen, J., Huang, W., 2011a. The effect
824 of laser scanning path on microstructures and mechanical properties of laser solid formed
825 nickel-base superalloy Inconel 718. *J. Alloys Compd* 509, 4505 – 4509. doi:[10.1016/j.](https://doi.org/10.1016/j.jallcom.2010.11.176)
826 [jallcom.2010.11.176](https://doi.org/10.1016/j.jallcom.2010.11.176).

827 Liu, F., Lin, X., Yang, G., Song, M., Chen, J., Huang, W., 2011b. Recrystallization and its
828 influence on microstructures and mechanical properties of laser solid formed nickel base
829 superalloy Inconel 718. *Rare Metals* 30, 433. doi:[10.1007/s12598-011-0319-0](https://doi.org/10.1007/s12598-011-0319-0).

830 Liu, Z., Kafka, O.L., Yu, C., Liu, W.K., 2018. Data-Driven Self-consistent Clustering Anal-
831 ysis of Heterogeneous Materials with Crystal Plasticity. volume 46. Springer International
832 Publishing. doi:[10.1007/978-3-319-60885-3_11](https://doi.org/10.1007/978-3-319-60885-3_11).

833 Maire, E., Bouaziz, O., Di Michiel, M., Verdu, C., 2008. Initiation and growth of damage
834 in a dual-phase steel observed by x-ray microtomography. *Acta Materialia* 56, 4954–4964.
835 doi:<https://doi.org/10.1016/j.actamat.2008.06.015>.

836 Maire, E., Carmona, V., Courbon, J., Ludwig, W., 2007. Fast X-ray tomography and
837 acoustic emission study of damage in metals during continuous tensile tests. *Acta Mater.*
838 55, 6806–6815. doi:[10.1016/j.actamat.2007.08.043](https://doi.org/10.1016/j.actamat.2007.08.043).

839 Markopoulos, A.P., Papazoglou, E.L., Karmiris-Obratański, P., 2020. Experimental Study
840 on the Influence of Machining Conditions on the Quality of Electrical Discharge Machined
841 Surfaces of aluminum alloy Al5052. *Machines* 8, 1–12. doi:[10.3390/machines8010012](https://doi.org/10.3390/machines8010012).

842 McGinty, R.D., 2001. Multiscale Representation of Polycrystalline Inelasticity. Ph.D. thesis.
843 Georgia Tech.

- 844 Nguyen, T.T., Yvonnet, J., Bornert, M., Chateau, C., 2016. Initiation and propagation of
845 complex 3D networks of cracks in heterogeneous quasi-brittle materials: Direct comparison
846 between in situ testing-microCT experiments and phase field simulations. *J. Mech. Phys.*
847 *Solids* 95, 320–350. doi:[10.1016/j.jmps.2016.06.004](https://doi.org/10.1016/j.jmps.2016.06.004).
- 848 Ning, F., Hu, Y., Liu, Z., Wang, X., Li, Y., Cong, W., 2018. Ultrasonic vibration-assisted
849 laser engineered net shaping of Inconel 718 parts: Microstructural and mechanical char-
850 acterization. *J. Manuf. Sci. Eng.* 140. doi:[10.1115/1.4039441](https://doi.org/10.1115/1.4039441). 061012.
- 851 Parimi, L.L., Attallah, M.M., Gebelin, J., Reed, R.C., 2012. Direct Laser Fabrication of
852 Inconel-718: Effects on Distortion and Microstructure. John Wiley and Sons, Ltd. pp. 509
853 – 519. doi:[10.1002/9781118516430.ch56](https://doi.org/10.1002/9781118516430.ch56).
- 854 Patterson, B.M., Cordes, N.L., Henderson, K., Xiao, X., Chawla, N., 2018. In situ Imaging
855 of Materials using X-ray Tomography. *Microsc. Microanal.* 24, 1002–1003. doi:[10.1017/
856 S1431927618005500](https://doi.org/10.1017/S1431927618005500).
- 857 du Plessis, A., Yadroitsava, I., Yadroitsev, I., 2020. Effects of defects on mechanical prop-
858 erties in metal additive manufacturing: A review focusing on X-ray tomography insights.
859 *Mater. Des.* 187, 108385. doi:[10.1016/j.matdes.2019.108385](https://doi.org/10.1016/j.matdes.2019.108385).
- 860 Qi, H., Azer, M., Ritter, A., 2009. Studies of standard heat treatment effects on microstruc-
861 ture and mechanical properties of laser net shape manufactured INCONEL 718. *Metall.*
862 *Mat. Trans. A* 40, 2410–2422. doi:[10.1007/s11661-009-9949-3](https://doi.org/10.1007/s11661-009-9949-3).
- 863 Samei, J., Amirmaleki, M., Ventura, A.P., Pawlikowski, G.T., Bayes, M., Misiolek, W.Z.,
864 Wilkinson, D.S., 2020. In-situ X-ray tomography analysis of the evolution of pores during
865 deformation of a Cu-Sn alloy fabricated by selective laser melting. *Addit. Manuf.* 34,
866 101196. doi:[10.1016/j.addma.2020.101196](https://doi.org/10.1016/j.addma.2020.101196).
- 867 Schneider, J., 2020. Comparison of Microstructural Response to Heat Treatment of Inconel

868 718 Prepared by Three Different Metal Additive Manufacturing Processes. JOM 72, 1085–
869 1091. doi:[10.1007/s11837-020-04021-x](https://doi.org/10.1007/s11837-020-04021-x).

870 Shamsaei, N., Yadollahi, A., Bian, L., Thompson, S.M., 2015. An overview of Direct Laser
871 Deposition for additive manufacturing; Part II: Mechanical behavior, process parameter
872 optimization and control. Addit. Manuf. 8, 12–35. doi:[10.1016/j.addma.2015.07.002](https://doi.org/10.1016/j.addma.2015.07.002).

873 Small, K.B., Englehart, D.A., Christman, T.A., . A guide to etching specialty alloys
874 for microstructural evaluation. URL: [https://www.carpentertechnology.com/blog/
875 a-guide-to-etching-specialty-alloys](https://www.carpentertechnology.com/blog/a-guide-to-etching-specialty-alloys).

876 Sochalski-Kolbus, L.M., Payzant, E.A., Cornwell, P.A., Watkins, T.R., Babu, S.S., Dehoff,
877 R.R., Lorenz, M., Ovchinnikova, O., Duty, C., 2015. Comparison of Residual Stresses
878 in Inconel 718 Simple Parts Made by Electron Beam Melting and Direct Laser Metal
879 Sintering. Metall. Mater. Trans. A 46, 1419–1432. doi:[10.1007/s11661-014-2722-2](https://doi.org/10.1007/s11661-014-2722-2).

880 Steuwer, A., Daniels, J.E., 2011. In-situ stress and strain measurements around cracks
881 using synchrotron X-ray diffraction. J. Strain Anal. Eng. Des. 46, 593–606. doi:[10.1177/
882 0309324711408501](https://doi.org/10.1177/0309324711408501).

883 Steuwer, A., Edwards, L., Pratihari, S., Ganguly, S., Peel, M., Fitzpatrick, M.E., Marrow,
884 T.J., Withers, P.J., Sinclair, I., Singh, K.D., Gao, N., Buslaps, T., Buffière, J.Y., 2006.
885 In situ analysis of cracks in structural materials using synchrotron X-ray tomography and
886 diffraction. Nucl. Instrum. Methods Phys. Res. 246, 217–225. doi:[10.1016/j.nimb.2005.
887 12.063](https://doi.org/10.1016/j.nimb.2005.12.063).

888 Sui, S., Tan, H., Chen, J., Zhong, C., Li, Z., Fan, W., Gasser, A., Huang, W., 2019. The
889 influence of Laves phases on the room temperature tensile properties of Inconel 718 fab-
890 ricated by powder feeding laser additive manufacturing. Acta Mater. 164, 413 – 427.
891 doi:[10.1016/j.actamat.2018.10.032](https://doi.org/10.1016/j.actamat.2018.10.032).

892 Toda, H., Maire, E., Aoki, Y., Kobayashi, M., 2011. Three-dimensional strain mapping
893 using in situ X-ray synchrotron microtomography. *J. Strain Anal. Eng. Des.* 46, 549–561.
894 doi:[10.1177/0309324711408975](https://doi.org/10.1177/0309324711408975).

895 VIC-2D Version 6, Correlated Solutions, Irmo SC, [https://www.correlatedsolutions.com/vic-](https://www.correlatedsolutions.com/vic-2d/)
896 [2d/](https://www.correlatedsolutions.com/vic-2d/), .

897 Voisin, T., Calta, N.P., Khairallah, S.A., Forien, J.B., Balogh, L., Cunningham, R.W.,
898 Rollett, A.D., Wang, Y.M., 2018. Defects-dictated tensile properties of selective laser
899 melted Ti-6Al-4V. *Mater. Des.* 158, 113–126. doi:[10.1016/j.matdes.2018.08.004](https://doi.org/10.1016/j.matdes.2018.08.004).

900 Watring, D.S., Benzing, J.T., Kafka, O.L., Liew, L.A., Moser, N.H., Erickson, J., Hrabe, N.,
901 Spear, A.D., 2022. Evaluation of a modified void descriptor function to uniquely char-
902 acterize pore networks and predict fracture-related properties in additively manufactured
903 metals. *Acta Materialia* 223, 117464. doi:[10.1016/j.actamat.2021.117464](https://doi.org/10.1016/j.actamat.2021.117464).

904 Weck, A., Wilkinson, D., Maire, E., Toda, H., 2008. Visualization by x-ray tomography of
905 void growth and coalescence leading to fracture in model materials. *Acta Materialia* 56,
906 2919–2928. doi:<https://doi.org/10.1016/j.actamat.2008.02.027>.

907 Wejdemann, C., Lienert, U., Pantleon, W., 2010. In situ measurements of X-ray peak profile
908 asymmetry from individual grains. *J. Phys.: Conference Series* 240, 012160. doi:[10.1088/
909 1742-6596/240/1/012160](https://doi.org/10.1088/1742-6596/240/1/012160).

910 Wolff, S.J., Gan, Z., Lin, S., Bennett, J.L., Yan, W., Hyatt, G., Ehmann, K.F., Wagner,
911 G.J., Liu, W.K., Cao, J., 2019. Experimentally validated predictions of thermal history
912 and microhardness in laser-deposited Inconel 718 on carbon steel. *Addit. Manuf.* 27,
913 540–551. doi:[10.1016/j.addma.2019.03.019](https://doi.org/10.1016/j.addma.2019.03.019).

914 Xavier, M.S., Yang, S., Comte, C., Bab-Hadiashar, A., Wilson, N., Cole, I., 2020. Nonde-
915 structive quantitative characterisation of material phases in metal additive manufacturing

916 using multi-energy synchrotron X-rays microtomography. *Int. J. Adv. Manuf. Technol.*
917 106, 1601–1615. doi:[10.1007/s00170-019-04597-y](https://doi.org/10.1007/s00170-019-04597-y).

918 Yan, W., Lian, Y., Yu, C., Kafka, O.L., Liu, Z., Liu, W.K., Wagner, G.J., 2018. An
919 integrated process–structure–property modeling framework for additive manufacturing.
920 *Comput. Methods Appl. Mech. Eng* 339, 184–204. doi:[10.1016/j.cma.2018.05.004](https://doi.org/10.1016/j.cma.2018.05.004).

921 Yu, C., 2019. *Multiscale Clustering Analysis*. Phd. Northwestern University.

922 Yu, C., Kafka, O.L., Liu, W.K., 2019. Self-consistent clustering analysis for multiscale
923 modeling at finite strains. *Comput. Methods Appl. Mech. Eng.* 349, 339–359. doi:[10.1016/j.cma.2019.02.027](https://doi.org/10.1016/j.cma.2019.02.027).

925 Yuan, K., Guo, W., Li, P., Wang, J., Su, Y., Lin, X., Li, Y., 2018. Influence of process
926 parameters and heat treatments on the microstructures and dynamic mechanical behaviors
927 of Inconel 718 superalloy manufactured by laser metal deposition. *Mater Sci. Eng, A* 721,
928 215 – 225. doi:[10.1016/j.msea.2018.02.014](https://doi.org/10.1016/j.msea.2018.02.014).

929 Yvell, K., Grehk, T.M., Hedström, P., Borgenstam, A., Engberg, G., 2018. Microstructure
930 development in a high-nickel austenitic stainless steel using EBSD during in situ tensile
931 deformation. *Mater. Charact.* 135, 228–237. doi:[10.1016/j.matchar.2017.11.046](https://doi.org/10.1016/j.matchar.2017.11.046).

932 Zhai, Y., Lados, D.A., Brown, E.J., Vigilante, G.N., 2019. Understanding the microstructure
933 and mechanical properties of Ti-6Al-4V and Inconel 718 alloys manufactured by Laser
934 Engineered Net Shaping. *Addit. Manuf.* 27, 334 – 344. doi:[10.1016/j.addma.2019.02.](https://doi.org/10.1016/j.addma.2019.02.017)
935 [017](https://doi.org/10.1016/j.addma.2019.02.017).

936 Zhang, Y., Yang, L., Lu, W., Wei, D., Meng, T., Gao, S., 2020. Microstructure and elevated
937 temperature mechanical properties of IN718 alloy fabricated by laser metal deposition.
938 *Mater. Sci. Eng, A* 771, 138580. doi:[10.1016/j.msea.2019.138580](https://doi.org/10.1016/j.msea.2019.138580).

939 Zhao, X., Chen, J., Lin, X., Huang, W., 2008. Study on microstructure and mechanical
940 properties of laser rapid forming Inconel 718. Mater. Sci. Eng, A 478, 119 – 124. doi:[10.1016/j.msea.2007.05.079](https://doi.org/10.1016/j.msea.2007.05.079).
941

942 Zhong, C., Gasser, A., Kittel, J., Wissenbach, K., Poprawe, R., 2016. Improvement of
943 material performance of Inconel 718 formed by high deposition-rate laser metal deposition.
944 Mater. Des 98, 128 – 134. doi:[10.1016/j.matdes.2016.03.006](https://doi.org/10.1016/j.matdes.2016.03.006).

945 **Appendix A. Crystallography**

946 The microstructure consisting of large columnar grains with high aspect ratio and a
947 preferred crystallographic orientation seems most prevalent, although a relatively small area
948 was sampled. Micro-Laue diffraction at APS beamline 34-ID-E was conducted on a small
949 region cut from the top corner of the thin wall, and Figure [A.21](#) shows two dominant features
950 from these measurements: first, similar elongated grains with a predominately orientated in
951 between the (101) and (001) directions is seen; second, the final layer of the build exhibits a
952 unique orientation, mostly (111), likely due to the lack of re-solidification during processing
953 of that layer (however, the this is supposition based on prior reports [Zhang et al. \(2020\)](#) and
954 direct evidence, for example from *in-situ* measurements, of this mechanism has not been
955 demonstrated to our knowledge). The existence of large, columnar, preferentially oriented
956 grains near where the test specimen were extracted from was corroborated with electron
957 backscatter diffraction (EBSD) measurements (not shown; available upon request).

958 **Appendix B. Detailed horizontal vs vertical data**

959 Figure [B.22\(a-c\)](#) shows a similar comparison for Young’s modulus between the vertical
960 and horizontal specimens for each processing condition. Figure [B.23\(a-c\)](#) compares the
961 0.2% offset yield stresses. Figure [B.24\(a-c\)](#) shows the ultimate tensile strengths, and Figure
962 [B.25\(a-c\)](#) shows a comparison of the elongation at failure (determined from the DIC data)
963 within each wall for both vertical and horizontal specimens. All sets of box-and-whisker

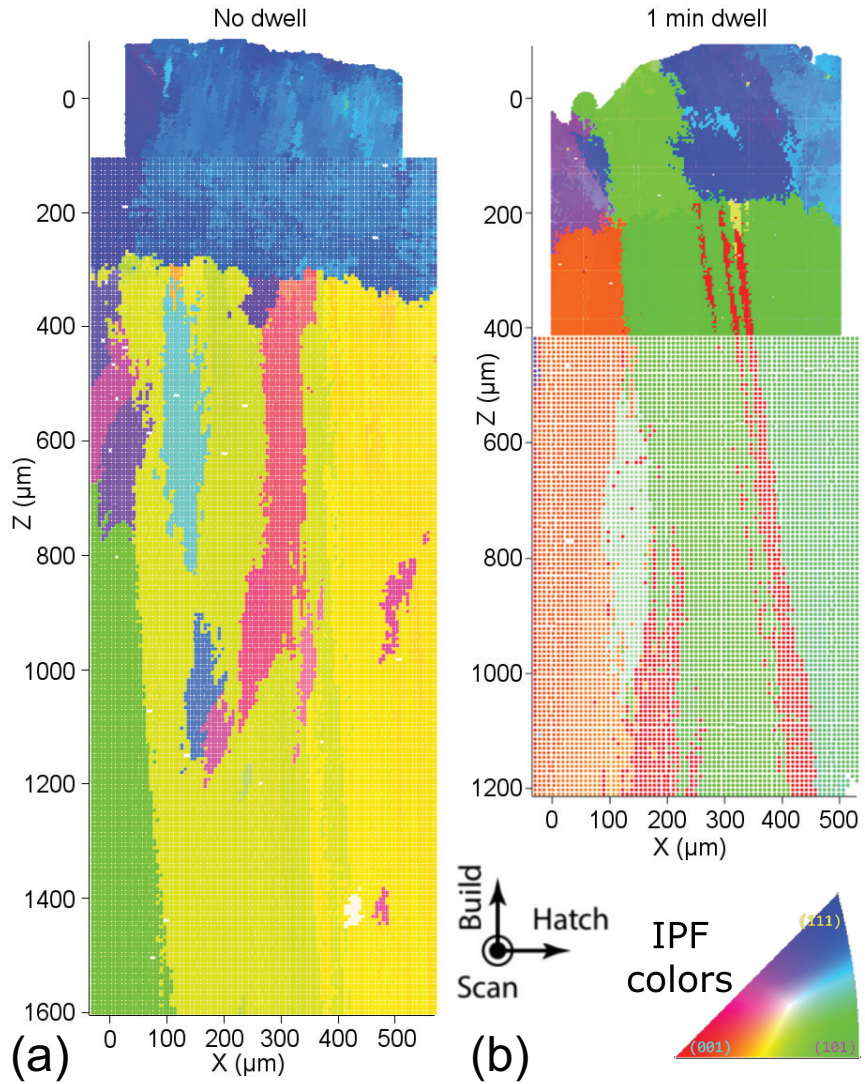


Figure A.21: X-ray micro-Laue diffraction (conducted at APS beamline 34-ID-E) images of the top corner of the no-dwell and one-minute dwell builds. Colored according to the IPF diagram. The apparent “grid” is a result of the visualization chosen to represent finite probe size during point-scanning.

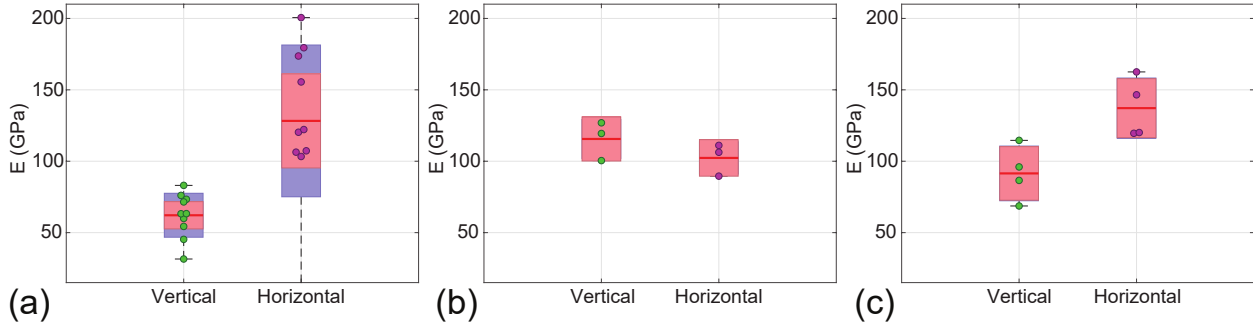


Figure B.22: Box-and-whisker plots showing the mean (red line), standard deviation (salmon region), 95% confidence interval (blue region), and extents (whiskers) of elastic modulus for (a) processing condition 1, (b) processing condition 2, (c) processing condition 3. Because modulus was measured before any of the stops, these all can be compared fairly. Individual green (vertical) or magenta (horizontal) points indicate individual tests (the points are moved slightly in the x-axis to be individually identifiable).

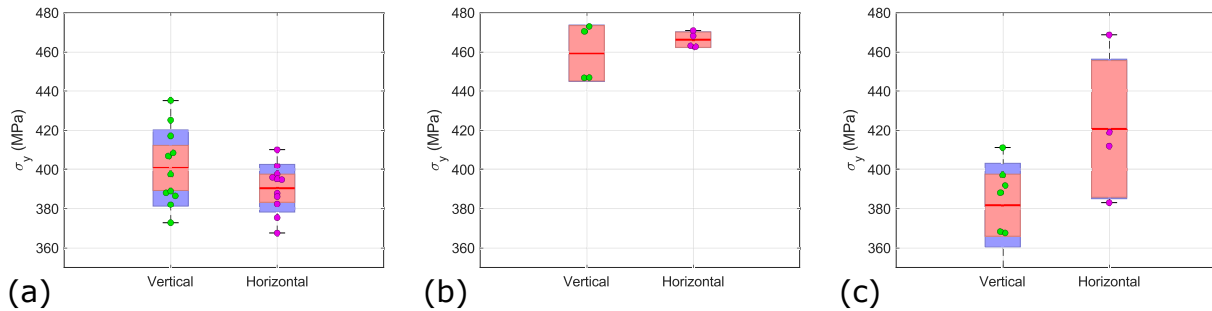


Figure B.23: Box-and-whisker plot showing the spread and mean values for yield stress for (a) processing condition 1, (b) processing condition 2, and (c) processing condition 3; in most cases, yield occurs before the first scan, so continuous and interrupted tests are generally comparable.

964 plots match the average trends observed in Figure 10, but provide more quantification of
 965 the specific values often used in engineering design. In each figure, the red line is the mean
 966 value, each dot represents an individual specimen, the salmon colored region represents one
 967 standard deviation (SD), the blue region represents a 95% confidence interval (CI), and the
 968 outliers are plotted on the whiskers. Note that these values (SD and CI) are intended for data
 969 that are normally distributed, but this is not necessarily true here because spatial variability
 970 is likely driven by non-random thermal conditions.

971 Appendix C. Detailed average pore deformation tables

972 Tabular data detailing all computed void descriptive measures averaged across all pores
 973 observed in each image. The notation $\langle \square \rangle_n$ indicates the number average of parameter

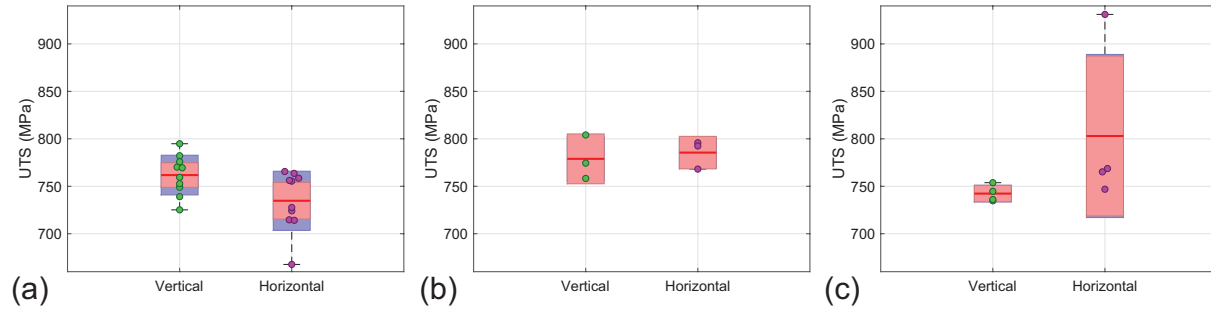


Figure B.24: A similar plot to Figure B.25, this time showing ultimate tensile strength for (a) processing condition 1, (b) processing condition 2, (c) processing condition 3. A mix of continuous and interrupted loading may make this comparison less reliable when comparing wall 1 (a) to walls 2 (b) and 3 (c).

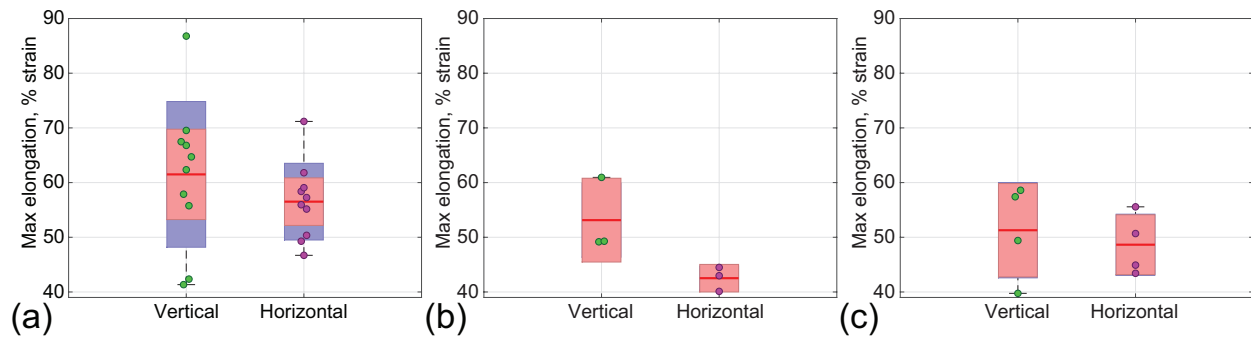


Figure B.25: Box-and-whisker plot showing maximum elongation for each specimen for (a) wall 1, (b) wall 2, (c) wall 3. Note that only walls 2 and 3 are necessarily directly comparable, because both are based on interrupted (stop-start) testing, whereas wall 1 was not.

Table C.5: H2-4 average pore data, all lengths in μm

Stress Level (MPa)	0	575	650	725	750	725	700
# pores	111	84	83	93	106	82	80
$\langle L \rangle_n$	12.19	12.07	12.05	12.24	12.22	14.13	13.7
$\langle W \rangle_n$	10.36	10.56	10.76	10.35	9.94	11.12	10.1
$\langle T \rangle_n$	8.41	8.44	8.68	8.54	7.85	7.82	7.5
$\langle L/T \rangle$	1.54	1.52	1.45	1.51	1.57	2.00	1.83
$\langle x \rangle$	10.38	10.38	10.32	9.76	8.93	11.49	9.05
σ_x	3.08	2.77	2.72	3.17	2.7	3.62	3.59
$\langle y \rangle$	11.54	11.34	11.18	10.82	10.01	10.80	10.26
σ_y	3.42	3.37	3.31	3.18	2.75	3.48	3.67
$\langle z \rangle$	8.19	8.37	8.94	9.36	10.25	10.44	11.7
σ_z	3.27	3.89	4.55	4.64	4.34	5.41	6.15

Table C.6: H3-4 average pore data, all lengths in μm

Stress Level (MPa)	0	575	650	725	700
# pores	274	311	301	245	267
$\langle L \rangle_n$	12.64	11.58	11.58	12.13	12.14
$\langle W \rangle_n$	9.10	8.67	8.63	8.99	8.79
$\langle T \rangle_n$	6.25	6.48	6.63	6.92	6.88
$\langle L/T \rangle$	2.16	1.93	1.87	1.84	1.83
$\langle x \rangle$	11.06	9.91	9.72	10.03	9.70
σ_x	3.57	2.99	2.88	2.97	2.97
$\langle y \rangle$	10.06	9.70	9.62	9.73	9.26
σ_y	2.32	2.31	2.39	2.69	2.29
$\langle z \rangle$	6.89	6.84	7.23	7.96	8.66
σ_z	3.01	2.98	3.24	3.39	3.7

974 \square , and $\sigma_{x,y,z}$ indicates first standard deviation of the extents x, y, and z.

975 Appendix D. Crystal Plasticity Modeling method

976 In this computational crystal plasticity implementation, the local deformation gradient
977 \mathbf{F} is multiplicatively decomposed into elastic \mathbf{F}^e and inelastic \mathbf{F}^{in} contributions:

$$\mathbf{F} = \mathbf{F}^e \cdot \mathbf{F}^{\text{in}}. \quad (\text{D.1})$$

978 The inelastic deformation gradient \mathbf{F}^{in} can be determined using a plastic constitutive law to
979 relate the plastic velocity gradient $\mathbf{L}^p = \dot{\mathbf{F}}^p \cdot (\mathbf{F}^p)^{-1}$ to the plastic shear rate $\dot{\gamma}^\alpha$ across all

Table C.7: V2-4 average pore data, all lengths in μm

Stress Level (MPa)	0	575	650	725	800	775	750
# pores	391	175	183	190	102	128	103
$\langle L \rangle_n$	14.73	14.02	13.56	13.94	13.07	14.15	14.31
$\langle W \rangle_n$	10.63	10.72	10.39	10.43	10.61	10.39	10.23
$\langle T \rangle_n$	7.91	8.00	8.31	8.01	8.75	8.39	8.18
$\langle L/T \rangle$	1.93	1.89	1.71	1.87	1.5	1.66	1.7
$\langle x \rangle$	12.65	12.21	11.37	11.84	10.1	9.66	9.20
σ_x	4.62	4.71	4.3	4.16	3.34	2.94	2.82
$\langle y \rangle$	10.78	10.56	11.04	10.67	10.87	10.34	10.39
σ_y	3.12	3.39	3.14	2.86	3.07	3.27	3.1
$\langle z \rangle$	9.65	9.30	9.33	9.35	10.66	12.22	12.67
σ_z	4.52	4.56	4.32	4.64	5.92	7.28	7.55

Table C.8: V3-4 average pore data, all lengths are in μm

Stress level (MPa)	0	575	650	725	600	675	650	Failed
# pores	236	159	164	164	158	159	163	182
$\langle L \rangle_n$	11.52	12.15	12.08	11.86	12.41	12.32	12.40	13.01
$\langle W \rangle_n$	8.62	9.16	9.20	9.19	9.55	9.36	9.35	9.36
$\langle T \rangle_n$	7.00	7.34	7.36	7.46	7.52	7.42	7.33	7.16
$\langle L/T \rangle$	1.73	1.88	1.73	1.65	1.7	1.73	1.81	1.86
$\langle x \rangle$	8.96	9.90	9.26	9.03	9.35	9.13	9.16	8.91
σ_x	3.07	4.74	3.9	2.88	3.83	3.76	3.49	3.35
$\langle y \rangle$	9.74	10.20	10.24	9.86	9.94	9.79	9.65	9.74
σ_y	2.37	3.4	3.31	2.75	3.28	3.16	2.69	2.82
$\langle z \rangle$	7.91	7.94	8.59	8.86	9.51	9.53	9.63	10.55
σ_z	2.61	3.21	3.4	3.81	4.85	4.65	4.82	4.97

980 slip systems $1 \dots \alpha$ through

$$\mathbf{L}^p = \sum_{\alpha=1}^{N_{\text{slip}}} \dot{\gamma}^{\alpha} (\mathbf{s}_0^{\alpha} \otimes \mathbf{n}_0^{\alpha}). \quad (\text{D.2})$$

981 Here, \mathbf{s}_0^{α} and \mathbf{n}_0^{α} are unit vectors that define the slip direction and slip plane normal for slip
 982 system α in the undeformed configuration, N_{slip} is the number of active slip systems, and \otimes
 983 is the dyadic product. In general, the plastic shear rate $\dot{\gamma}^{\alpha}$ in slip system α is taken to be
 984 a function of resolved shear stress τ^{α} , deformation resistance τ_0^{α} , and back stress a^{α} in that
 985 slip system. The resolved shear stress is given by

$$\tau^{(\alpha)} = \boldsymbol{\sigma} : (\mathbf{s}^{\alpha} \otimes \mathbf{n}^{\alpha}), \quad (\text{D.3})$$

986 where $\boldsymbol{\sigma}$ is the Cauchy stress, $\mathbf{s}^{(\alpha)}$ is the slip direction, and $\mathbf{n}^{(\alpha)}$ is the slip plane normal, all of
 987 which are defined in the deformed configuration. They are computed from their counterparts
 988 in the undeformed configuration with

$$\begin{cases} \boldsymbol{\sigma} = \frac{1}{J_e} [\mathbf{F}^e \cdot \mathbf{S}^e \cdot (\mathbf{F}^e)^T], \\ \mathbf{s}^{\alpha} = \mathbf{F}^e \cdot \mathbf{s}_0^{\alpha}, \\ \mathbf{n}^{\alpha} = \mathbf{n}_0^{\alpha} \cdot (\mathbf{F}^e)^{-1}. \end{cases} \quad (\text{D.4})$$

989 The evolution law for $\dot{\gamma}^{\alpha}$ is given by

$$\dot{\gamma}^{\alpha} = \dot{\gamma}_0 \left| \frac{\tau^{\alpha} - a^{\alpha}}{\tau_0^{\alpha}} \right|^{(\tilde{m}-1)} \left(\frac{\tau^{\alpha} - a^{\alpha}}{\tau_0^{\alpha}} \right), \quad (\text{D.5})$$

990 where $\dot{\gamma}_0$ is a reference shear rate, and \tilde{m} is the exponent related to material strain rate
 991 sensitivity. The evolution laws for deformation resistance τ_0^{α} (the isotropic hardening term)

992 and back stress a^α (the kinematic hardening term) are given by McGinty [McGinty \(2001\)](#):

$$\begin{cases} \dot{\tau}_0^\alpha = H \sum_{\beta=1}^{N_{\text{slip}}} |\dot{\gamma}^\beta| - R\tau_0^\alpha \sum_{\beta=1}^{N_{\text{slip}}} |\dot{\gamma}^\beta|, \\ \dot{a}^\alpha = h\dot{\gamma}^\alpha - ra|\dot{\gamma}^\alpha| \end{cases} \quad (\text{D.6})$$

993 where H and h are direct hardening coefficients, and R and r are dynamic recovery coeffi-
994 cients. Note that in Eq. [\(D.6\)](#) we assume the latent hardening and self-hardening effects are
995 identical.